






# Flexible bioelectronic systems with large-scale temperature sensor arrays for monitoring and treatments of localized wound inflammation

Junhan Liu<sup>a,b,c,d</sup> , Zhongzheng Li<sup>a,c,d</sup>, Mubai Sun<sup>a,e</sup>, Lianjie Zhou<sup>a,c,d</sup>, Xiaojun Wu<sup>a,b,c</sup>, Yifei Lu<sup>a,c,d</sup>, Yuting Shao<sup>f</sup>, Chang Liu<sup>a,c,d</sup>, Ningge Huang<sup>a,b,c,d</sup>, Bofan Hu<sup>a,c,d</sup>, Zhongyuan Wu<sup>a,c,d</sup>, Chunyu You<sup>a,c,d</sup>, Lizhu Li<sup>g</sup>, Ming Wang<sup>b</sup>, Ling Tao<sup>h</sup>, Zengfeng Di<sup>i</sup>, Xing Sheng<sup>g,i,k</sup> , Yongfeng Mei<sup>a,c,d,1</sup>, and Enming Song<sup>a,b,c,d,1</sup> 

Affiliations are included on p. 11.

Edited by John Rogers, Northwestern University–Evanston, Evanston, IL; received June 21, 2024; accepted October 23, 2024

Continuous monitoring and closed-loop therapy of soft wound tissues is of particular interest in biomedical research and clinical practices. An important focus is on the development of implantable bioelectronics that can measure time-dependent temperature distribution related to localized inflammation over large areas of wound and offer in situ treatment. Existing approaches such as thermometers/thermocouples provide limited spatial resolution, inapplicable to a wearable/implantable format. Here, we report a conformal, scalable device package that integrates a flexible amorphous silicon-based temperature sensor array and drug-loaded hydrogel for the healing process. This system can enable the spatial temperature mapping at submillimeter resolution and high sensitivity of 0.1 °C, for dynamically localizing the inflammation regions associated with temperature change, automatically followed with heat-triggered drug delivery from hydrogel triggered by wearable infrared light-emitting-diodes. We establish the operational principles experimentally and computationally and evaluate system functionalities with a wide range of targets including live animal models and human subjects. As an example of medical utility, this system can yield closed-loop monitoring/treatments by tracking of temperature distribution over wound areas of live rats, in designs that can be integrated with automated wireless control. These findings create broad utilities of these platforms for clinical diagnosis and advanced therapy for wound healthcare.

temperature spatial mapping | wound inflammation | in situ therapy | closed-loop management | remote care

Technologies that enable swift, in vivo evaluations and management of wound tissues hold significant promise for extensive applications in biological research and clinical healthcare. Of particular interest are wearable/implantable systems that provide diagnostic value, track healing responses, and response to minor yet clinically meaningful deterioration across various inflammatory conditions (1–8). Sophisticated embodiments use materials/devices for in vivo characterization of wound physiological factors (e.g., pH, temperature, humidity) for guiding objective assessments of injury severity of inflammation such as external bacterial infections that impede the healing process (9–14). In all cases, a critical challenge is in the development of active bioelectronic systems that support closed-loop strategies (15–20), not only for large-scale mapping of physiological signals across wound tissues but also for automated therapy operation to promote healing, in an ideal scenario with wireless control. Technical requirements for these systems typically demand the use of flexible arrays of integrated electronic components at shape-conformal layouts (21–23). These forms should allow for high-quality, minimally invasive interfaces to soft, curvilinear, moving surfaces of living wound tissues, at levels of electrical performance approaching to those of conventional wafer-based forms of devices.

An important focus is dynamic mapping of temperature distribution across large-area wound surfaces, as the basis for localizing the infected region, assessing/grading the inflammation severity, and tracking of the wound-healing process, all of which involve changes in the temperature at spatial resolution within the wound site (24–27). Existing noninvasive approaches of temperature sensing for biological tissues include thermometers or thermocouples (28), typically with rigid, planar geometries that result in measurement uncertainties on highly curved tissue surfaces. Alternatives such as infrared technology can allow powerful capabilities of quantitative, spatial-temporal mapping of thermal distribution for a wide range of wound conditions. Recent reports have described the use of infrared cameras to identify and localize the inflammation region on wound tissues (29, 30). Although promising, these associated techniques necessitate additional equipment

## Significance

The emergence of high-performance bioelectronics designed to interface with wound tissues of the human body represents a breakthrough for medicine engineering, with capabilities of continuous monitoring of localized inflammation and closed-loop therapy. This work establishes the engineered materials, device designs, and integration schemes of biointegrated systems that incorporate both sensing and treatment components, for demonstrated utilities of wound managements in live animal models. Detailed in vivo studies yield quantitative temperature maps for dynamically localizing inflammation at submillimeter resolution over wound areas, followed by heat-triggered drug delivery for treatment processes. Integration with wireless programmable designs can enable such platforms with automated remote control. These findings provide clinical significance over previously reported technologies, with potential for wound medical managements of various conditions.

Copyright © 2024 the Author(s). Published by PNAS. This article is distributed under [Creative Commons Attribution-NonCommercial-NoDerivatives License 4.0 \(CC BY-NC-ND\)](https://creativecommons.org/licenses/by-nc-nd/4.0/).

<sup>1</sup>To whom correspondence may be addressed. Email: yfm@fudan.edu.cn or sem@fudan.edu.cn.

This article contains supporting information online at <https://www.pnas.org/lookup/suppl/doi:10.1073/pnas.2412423121/-/DCSupplemental>.

Published November 26, 2024.

and trained practitioners, thereby precluding the simple, rapid use as a fully wearable/implantable device architecture for continuous monitoring and stable operation while in direct contact to wound tissues and biofluids.

Emerging classes of bioelectronic devices can offer powerful possibilities in levels of functional integration. Examples take the forms ranging from conformal membranes to open network meshes (31–34), with distinct properties that distinguish from the past technologies owing to their capabilities of intimate interfaces to targeted tissues, biocompatible designs, and tissue-like mechanics. Recent research has established multifunctional wearable dressings on polymer substrates that characterize inflammation by detecting wound temperature and provide closed-loop treatments across healing timescale in a wired, nonautomated fashion (9, 35, 36). Constituent materials for temperature sensing typically include metal films, nanomesh/nanowires, and two-dimensional materials such as graphene (37–40). In many cases, however, these approaches typically provide limited performances with few sensing sites and poor resolution (centimeter to several millimeters level) across macroscopic wound areas (41–45), thus limiting their use for the precise, spatiotemporal mapping over large scales. Furthermore, preferable designs for closed-loop wound management feature wireless control, remote data capture and analysis, and fully automated therapy that can be activated during localized inflammation

The results present the development and applicability of a scalable device platform for monitoring inflammation and providing pharmacological therapy of wound tissues of the human body. These systems integrate components for sensing and treatments in a simple package, consisting of flexible arrays of amorphous silicon-based temperature sensors and drug-loaded hydrogel interfacing wound beds. Closed-loop operation includes spatial temperature mapping over large areas for localizing inflammation, automatically followed with drug delivery from hydrogel triggered by wearable infrared light-emitting-diode (IR-LED) array. The following sections highlight the engineered materials, device design and system integration, as stable interfaces for wound managements. Experimental and simulation studies demonstrate quantitative measurements of temperature, at submillimeter resolution and high sensitivity of 0.1 °C. Examples include proven utilities of living rats, with high-precision localization of inflammation sites and heat-controlled treatments. Integration of wireless circuits and programmable designs can yield system capabilities of wireless monitoring and temperature-enabled drug delivery in a fully automated fashion. These results create future opportunities for clinic use and at-home healthcare with continuous monitoring and treatment feedbacks of wound tissues.

## Results

**Materials, Designs, System Integration, and Operation Principles of Wound Optoelectronic Interfaces.** To enable high-performance, functional interfaces with large areas of wound tissues, we report the development and applicability of an array of flexible, wearable sensors and the associated optoelectronic platforms, which we refer to as an inflammation-monitoring-treatment (IMT) system. Fig. 1*A* presents the working principles of the IMT system as the basis of a stable wound tissue interface, as designed for identification of inflammation sites, simultaneously followed with timely treatments. Upon attaching the IMT system on the wound region, the temperature sensor array is capable of high-resolution monitoring for the changing surface temperature of large-scale wound tissues under dynamic conditions. An array of infrared light-emitting diodes (IR-LEDs) can subsequently

illuminate the inflamed regions and accurately elevate the localized temperature, thus resulting in the heat-triggered drug delivery from the underlying hydrogel. Here, a sol–gel transition occurs and releases the drug of penicillin (amoxicillin) from the hydrogel network for inflammation treatment, in parallel with decreasing temperature captured via the temperature sensor array for the following wound recovery.

The overall IMT system involves three functional layers from *Bottom* to *Top* (Fig. 1*B*): 1) an antibacterial hydrogel interface loaded with drug for inflammation treatment, 2) ultrathin amorphous silicon-based ( $\alpha$ -Si) temperature sensor array, and 3) the above IR-LED matrix for illumination of the heat-trigger process, encapsulated by the flexible silicone as cover layers to prevent external contamination in a biologically safe fashion. Specifically, the  $\alpha$ -Si temperature sensor array consists of 64 resistors (8 columns, 8 rows), each with dimensions of 400  $\mu\text{m}$  by 400  $\mu\text{m}$ , as shown in Fig. 1*B*, *i*, distributed uniformly over a total area of 12  $\times$  12  $\text{mm}^2$ . Each  $\alpha$ -Si sensor in nanomembrane forms (300 nm thick) incorporates two layers of metal interconnections that enable the capabilities of addressing for array sensing. A layer of film polyimide (PI) substrate (12  $\mu\text{m}$  thick) covers the entire bottom surface of the array, providing excellent heat transmissions for IR-LEDs and minimizing thermal cross talk between device units. The fabrication begins with definition of 64  $\alpha$ -Si channels on the PI substrate, followed by encapsulation of multiple layers of SU-8 photoresist (Microchem) for electrical insulation and to match the thermal expansion coefficient. A sequence of deposition of Cr/Au (10 nm/200 nm thick), etching, and photolithographic patterning forms the necessary metal connections for measurement readout. The total thickness of the temperature sensor array is less than 20  $\mu\text{m}$ , thus yielding an ultrathin structure with exceptional flexibility and conformability. Experimental details can be found in *SI Appendix, Text S1*.

In addition to the temperature sensor array, Fig. 1*B*, *ii* shows the specially formulated antibacterial hydrogel layer embedded with amoxicillin and interfacing with the biological tissue. Such platforms not only provide mechanical compliance in contact with soft time-dynamic wound tissues with breathability and adhesiveness but also serve as the carrier to transport chemical drug for subsequent treatments. The composition of the hydrogel is engineered to undergo sol–gel transition under the heat generated by the IR-LEDs, thereby facilitating targeted drug release. The fabrication includes the dissolution of gelatin and amoxicillin, cross-linking, and casting (*SI Appendix, Fig. S1 and Text S2*). As for heating units, a 2  $\times$  2 array of surface-mounted IR-LEDs is connected via reflow soldering onto a customized flexible substrate of PI. The IR-LEDs are distributed uniformly, each of which is responsible for localized heating of a corner. Detailed information on the device fabrication can be found in *SI Appendix, Text S3*. As an alternative substrate for better breathability than silicone, the application of Tegaderm film (25  $\mu\text{m}$  thick, 3 M) can provide excellent moisture and vapor exchange [with a moisture vapor transmission rate (MVTR) of  $\sim$ 800  $\text{g}/\text{m}^2/\text{day}$ , 46] compared to those of silicone (with a MVTR of  $\sim$ 50  $\text{g}/\text{m}^2/\text{day}$ , 47). *SI Appendix, Fig. S2*, shows that the application of Tegaderm film as the substrate of the entire device structure of the IMT systems can yield an intimate biotic/abiotic interface on human skins of the forearm as an example and simultaneously provide stable device performance, results of which have also been widely used in other publications (48, 49).

Fig. 1*C* demonstrates the optical images for the functional layers, i.e., temperature sensor array, IR-LED array, and hydrogel patch, without encapsulation of the silicone cover layer. The entire device is finally encapsulated with ultraflexible silicone to complete the final assembly, where the overall thickness of 1 mm of the IMT

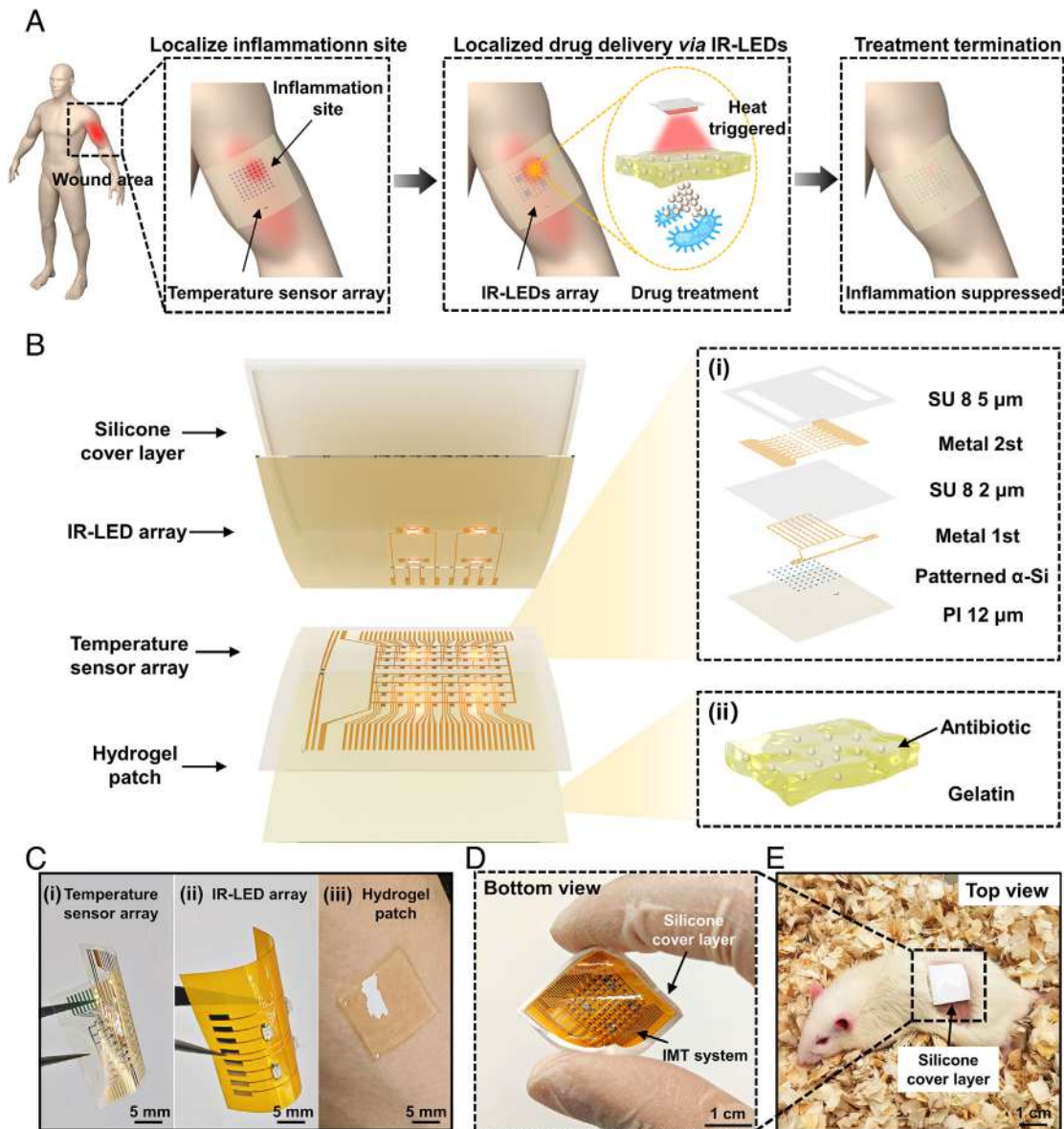


**Fig. 1.** Design, structure, and functional schematic of IMT systems for inflammation monitoring and treatment. (A) Schematic diagram of the operation of IMT systems: The temperature sensor array detects a local temperature increase in the inflamed area, activating the IR-LED for in situ heat-triggered drug release from the hydrogel until inflammation is suppressed. (B) Exploded view illustration of the IMT systems: (i) exploded view illustration of the temperature sensor layer and (ii) enlarged view of the drug-loaded hydrogel. (C) Optical images of the three functional sections: (i) temperature sensor array, (ii) IR-LED array, and (iii) hydrogel patch, all without encapsulation of silicone cover layer. (D) Optical image of the fully assembled IMT system by the silicone cover layer from *Bottom* view. (E) Photograph of the IMT system with silicone cover layer seamlessly attached on the skin of the rat, as for a *Top* view.

system is compatible with those of multifunctional wound dressings reported before (16, 20 and Fig. 1D). Due to the selection of biocompatible soft materials for the construction of the various layers, the smart wound dressing interface (area of  $22 \times 22 \text{ mm}^2$ ) offers excellent flexibility and biocompatibility, allowing it to form conformal contact with the surface of biological entities (Fig. 1E and *SI Appendix, Fig. S3 and Text S4*). Here, as the top part, the protective layer of the silicone cover layer can encapsulate the entire IMT system and thus prevent movement or delamination of devices during long-term operation. Notably, such a fabrication process is capable of scaling up to wafer dimensions, thereby allowing for systems that provide full-area coverage across most of the wound tissues of the human body (*SI Appendix, Fig. S4*).

**Device Characteristics of IMT Systems for Wound Optoelectronic Interfaces.** Monitoring the temperature distribution across the wound region can provide diagnostic utility, where the

inflammation generally results in a localized change of temperature (typically refers to an increase by  $2^\circ\text{C}$ ) (29, 50, 51). Of particular interest are advanced optoelectronic systems that can enable high-resolution measurements of temperature over wound tissues, track response to treatment, and evaluate for small but clinically meaningful deterioration for a wide range of pathophysiologic conditions. Fig. 2A shows the optical image of the temperature sensor array coupled on a curved surface, as the basis of the sensing platform of the IMT system. Here, the  $\alpha$ -Si sensor, in nanomembrane forms (*SI Appendix, Fig. S5*), can serve effectively as pixelated electronic components that yield high-resolution network matrix upon electrical interconnection, thus offering high-precision measurement of the temperature across large scales of wound surfaces (Fig. 2B and *SI Appendix, Figs. S6 and S7*).

Results in Fig. 2C exhibit that the conductive resistance of a representative unit sensor is negatively correlated with temperature, following the Arrhenius law which can be expressed as Eq. 1.

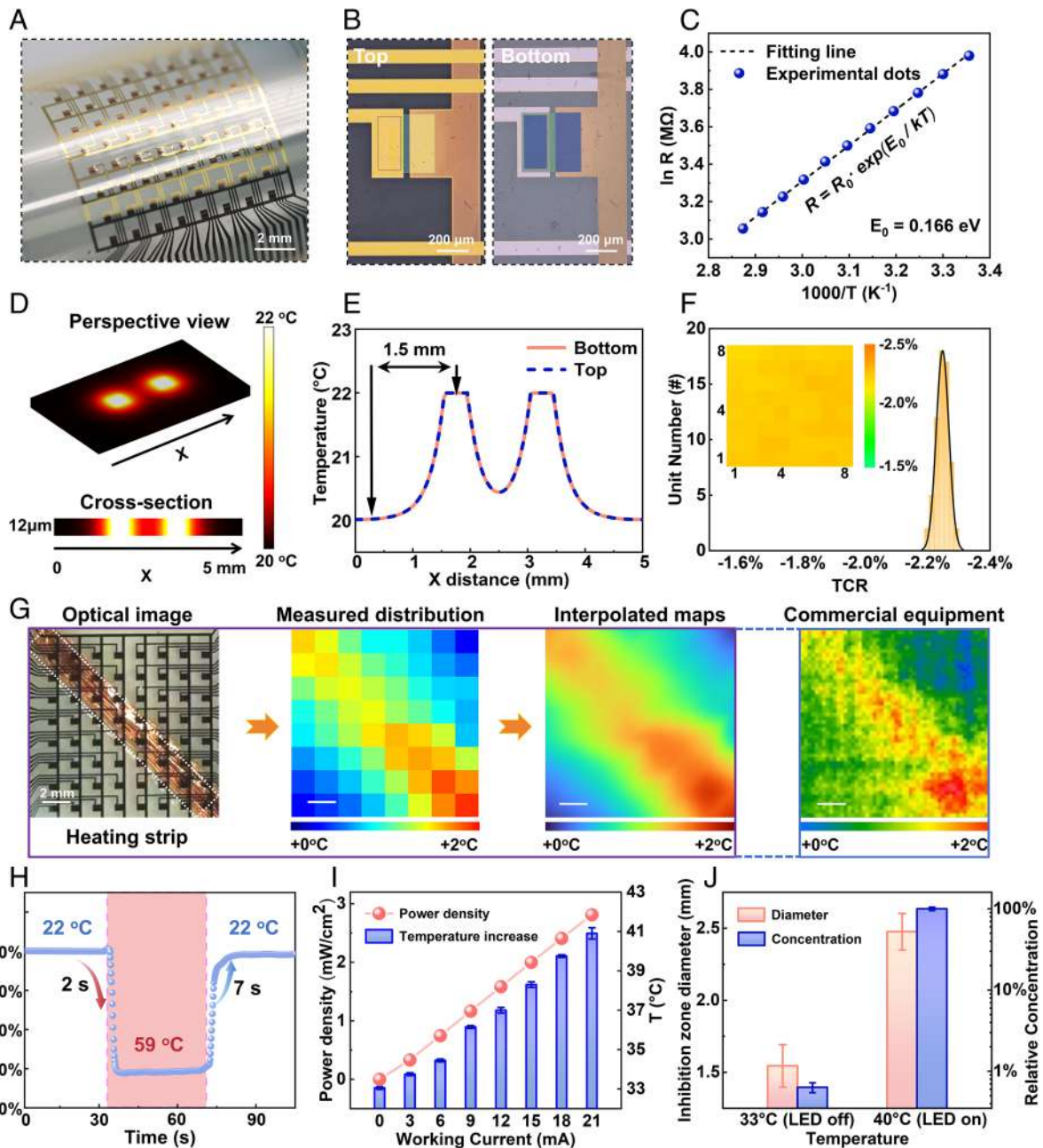


**Fig. 2.** Device performance characterization of the IMT system. (A) Photograph of the temperature sensor array attached on a curving surface. (B) Photograph of the top and bottom sides of a single device unit. (C) Measured sensor resistance in function of temperature (blue dots) and fitted Arrhenius plot (black dash line). (D and E) FEA simulation of the array layout without thermal signal cross talk. The influence of heat diffusion can be neglected. (F) Histogram (with Gaussian line shape fitting) of TCR from an array of 64 channels. The results indicate 100% yield and uniform TCR values. The *Inset* is a spatial map of TCR values. (G) Thermal imaging of the simulating skin inflammation, with interpolation fitting optimization results consistent with those of a commercial infrared camera. (H) Transient response performance of the temperature sensor. (I) The output power density and temperature of the IR-LEDs in function of working current. (J) Diameter of the antibacterial zone and concentration of the released drug below and at the hydrogel drug-release temperature.

Furthermore, performing a differential on Eq. 1 can infer the expression of temperature coefficient of resistance (TCR) defined as percentage change in resistance per Kelvin as Eq. 2:

$$R = R_0 \cdot \exp\left(\frac{E_0}{kT}\right), \quad [1]$$

$$\text{TCR} = \frac{1}{R} \cdot \frac{dR}{dT} = -\frac{E_0}{kT^2}, \quad [2]$$

where  $T$  is the temperature in Kelvin,  $k$  is the Boltzmann constant,  $E_0$  is the activation energy of the carriers, and  $R_0$  is the resistance

at infinite temperature. The activation energy  $E_0$  of the  $\alpha$ -Si sensor computed from the Arrhenius plot is 0.166 eV. The TCR of the  $\alpha$ -Si sensor at 37 °C is then calculated to be negative as -2.00%, which is consistent with the experimental value (-1.96%) and an order of magnitude larger than those of noble metal materials (e.g., Au, Pt) (52, 53). The temperature sensitivity can reach as low as 0.1 °C by analysis of the SD of resistance value (*SI Appendix, Fig. S8*). Experimental details can be found in *SI Appendix, Text S5*. In addition to the temperature sensing, the  $\alpha$ -Si sensor remains stable electrical performance under both illumination and dark conditions, with a negligible photoconductive effect that excludes the influence induced by the infrared light from the above IR-LEDs (*SI Appendix, Fig. S9*).

In order to examine the measurement cross talk within the array, finite element analysis (FEA) using COMSOL Multiphysics can quantify the heat coupling between two nearby  $\alpha$ -Si sensors (Fig. 2D). The distribution of equivalent temperature across the two adjacent units of sensors appears in Fig. 2E, for the case of measurements (22 °C within inflammation spots; 20 °C for room temperature), with the sensors on a PI film (12  $\mu$ m thick). The measured temperatures between the two adjacent sensors with a spacing distance of 1.5 mm can be distinguished from each other, yielding a temperature cross talk of 0.02 °C that is lower by orders of magnitude than those of the typical temperature change at wound tissues (approximately 2 °C). Specifically, the thermal insulation properties of the PI film (thermal conductivity approximately 0.2 W/m k) effectively prevent thermal interference among neighboring sensors during operation, and its thin-film profile ensures that the temperature distribution of the top and bottom sides is the same. Detailed information appears in *SI Appendix, Text S6*.

For the in vitro assessment of electrical performance, Fig. 2F displays the histogram plots of the TCR measured on all 64 unit channels of a representative array device. Such an array matrix offers a yield of 100% and a mean per-channel TCR of -2.25% (median: -2.25%). The yield here is defined as the number of working sites divided by the number of total sensing units from the array. The TCR remains nearly consistent within a narrow temperature span, averaging around -2.25% within the 30 °C to 45 °C range and adhering to a Gaussian distribution with a coefficient of variation at 0.9%. Cumulative statistics on the average TCR magnitudes and yields indicate high levels of uniformity and reproducibility across the entire array that can be achieved routinely. Additional experiments to demonstrate the sensitivity and accuracy of temperature sensors across a 1-mo timescale show minor changes of electrical resistance, TCR, and accuracy (defined as the SD of the resistance values at a constant room temperature divided by TCR), indicating minor signal drifts for temperature measurements over 1 mo (*SI Appendix, Fig. S10*).

Fig. 2G presents an example of in vitro thermal imaging using the  $\alpha$ -Si sensor array on artificial skin substrates of PDMS films (1 mm thick). Detailed calibration methods for each sensor in the array appear in *SI Appendix, Text S7*. In order to simulate heat generating from inflammation, strip heat source (white frame on *Left* of Fig. 2G) underlying the PDMS film can mimic the heat distribution across wound tissues. More details and experimental settings appear in *SI Appendix, Fig. S11*. From *Left to Right* in Fig. 2G, the temperature values of each pixel are captured using a representative device array, resulting in a spatial map for pixelated temperature field distribution (400  $\mu$ m). Further optimization *via* bicubic interpolation method (*SI Appendix, Code S1*), commonly used in clinical settings (54), can yield a thermal imaging of the high-resolution interpolated map. The *Right Inset* of Fig. 2G demonstrates the two-dimensional spatial map of surface temperature captured using a commercial infrared thermal-imaging camera (Seek Thermal) for the same case. As a comparison, the results of the temperature sensor array of IMT systems are in good agreement with the gold standard for thermal imaging utility. More targets including the human body can be seen in *SI Appendix, Figs. S12–S14*. Notably, *SI Appendix, Fig. S15*, exhibits that the temperature sensor array of the IMT system after 1-mo use can precisely measure external heating source and rebuild the temperature profile during the in vitro test, with measurement results in good agreement with those measured by commercial IR camera, indicating the ideal service life of the IMT system for routine application.

Beyond the quasi-static conditions, the sensor can enable time-dependent measurements of temperatures under dynamic condi-

tions. Fig. 2H records the ratio of R and  $R_0$  (original resistance) of a representative sensor as a function of time, dynamically measuring the change of electrical resistance of the sensor in response to the variation of target temperature. Experimental details appear in the *Materials and Methods* section. During the dynamic sensing, the sensor displays a rapid measurement response time of 2 s and of 7 s for the increase and decrease of temperature, respectively. Compared to the relatively long-term duration for wound inflammation and recovery (i.e., several days), we can thus neglect such short response time of the temperature sensor for spatial mapping of wound tissues. Furthermore, the device stability under exposure to biofluids is proven by exposure tests at 37 °C, results of which show excellent endurance for biofluids over 15 d that surpass the duration of the wound healing process, without significant changes of the average relative electrical resistance and TCR (*SI Appendix, Fig. S16*). Accelerated tests at higher temperature (96 °C) indicate the failure mechanism (*SI Appendix, Fig. S17A*), with a sudden failure with device yield down to 0% after 2 d (red dots) compared to stable performance at 37 °C (blue dots). *SI Appendix, Fig. S17B*, collects the I-V curves of a representative temperature sensor from the array across 3-d soaking at 96 °C. Results show that the vapor and biofluid permeation through the PI layers can yield increase of resistance of sensors, and eventually lead to failure of  $\alpha$ -Si-based sensors (55). Experimental details can be found in *SI Appendix, Text S8*.

To simulate the prolonged wear conditions, results in *SI Appendix, Fig. S18*, illustrate the device performance under cyclic bending tests, where the measured electrical resistance and TCR from the representative sensor array before/after 1,000-cycle bending test remain stable, with very minor changes for each parameter (<0.4%), indicating that the measurement sensitivity of our flexible devices remains stable under dynamic mechanical conditions, also consistent with the results of previous studies (34, 44, 56). Such robustness satisfies the demands for routine temperature monitoring continuously on biological entities without notable performance degradation.

Advanced wound care strategies are supposed to integrate both monitoring and treatment capabilities to streamline patient care by combining diagnostics and therapeutics. Fig. 2I illustrates power densities of the IR-LEDs (peak wavelength of 850 nm) under different working states for heat generation. The wearable application of an on-state of IR-LED can yield a maximum operation temperature of ~40 °C at the central region, assessed by the use of a commercial IR camera, results of which are biocompatible to biological tissues in a safe temperature range (57, 58 and *SI Appendix, Fig. S19* and *Table S1*). Furthermore, the *Inset* of *SI Appendix, Fig. S19*, demonstrates four IR-LEDs all with on-states on the forearm, consistent with localized heat of the individual IR-LED. These findings suggest that the heat generated by our IMT systems is in a biologically safe fashion. As the working current increases, the power density of IR-LEDs increases in accordance with a linear relationship, generates extra heat, and therefore raises the localized temperature to drive the underlying hydrogel to release the drug for treatment of wound tissues. In this manner, IR-LEDs that serve as reliable heat sources can allow for precise temperature control to thermally activate the drug delivery for targeted therapeutic actions (*SI Appendix, Figs. S20* and *S21*). In addition to the heat source, the sol-gel transition trend of the thermal responsive hydrogel enables relevant drug release based on the Korsmeyer-Peppas (K-P) modeling (59, 60), of which the mechanism and kinetics are discussed in *SI Appendix, Fig. S22* and *Text S9*. Fig. 2J presents that the amount of penicillin released and diameter of inhibition zone during on-state temperature (40 °C) of IR-LEDs surpasses that of off-state temperature (33 °C), indicating efficient

heat-triggered drug release activity correlated to variable working states of IR-LEDs (*SI Appendix, Figs. S23 and S24 and Text S10*). Besides, the stability of the hydrogel patch is further demonstrated by simulated wearing on fresh and clean pork skin (*Inset in SI Appendix, Fig. S25A*), in conditions of constant temperature (33 °C) and high humidity (85%). The stable weight of the hydrogel patch during 3 d indicates a saturation hydration degree and no degradation of gelatin (*SI Appendix, Fig. S25A*). In addition, the drug-loaded hydrogel patches w/o 3-d attachment on pork skin exhibit the comparable antibacterial ability with inhibition zone diameters of 0.90 cm and 0.93 cm, respectively (*SI Appendix, Fig. S25B*). As a demonstration for biocompatibility assessments, we performed histological analysis that includes hematoxylin and eosin (H&E) staining and Masson's trichrome staining, with (*Left in SI Appendix, Fig. S26*) and without attachment of the IMT system (*Right in SI Appendix, Fig. S26*). Details appear in *SI Appendix, Text S11*. These findings indicate that the IMT system consisting of the temperature sensor array, IR-LEDs, and the antibacterial hydrogel layer can effectively enable as a unique tool for wound tissue studies, such as inflammation, recovery, and tissue regeneration, with the proven biocompatibility.

**Closed-Loop Monitoring and Treatment of IMT Systems for Wound Inflammation in Animal Models.** The IMT system can characterize the physiological information of wound tissues via monitoring of temperature variations associated with localized inflammations and enable drug release to infected regions for treatments. Fig. 3*A* shows the monitoring of wound information and on-demand treatment on an animal model of a living rat, with a large-area wound of centimeters on the back of the rat. Here, a digital multimeter (Keithley 2100) drives the entire system to real-time measure through the multichannel sensor array, while a source measure unit (NGI N2600) supplies the power of IR-LEDs for treatment feedback (*SI Appendix, Fig. S27*). Fig. 3*B* and *SI Appendix, Fig. S28*, show the optical image of the IMT system as the application to wound tissues. By comparison, a commercial infrared camera simultaneously provides the thermal imaging in parallel, with proven utilities to track the wound tissue temperatures on large scales.

For dynamically monitoring temperature across the wound area, Fig. 3*C* illustrates the sensor matrix distribution with their channel layouts, where a quarter of the area (orange frame) corresponds to the infected region by injecting inoculation with 20  $\mu\text{L}$  of  $10^6$

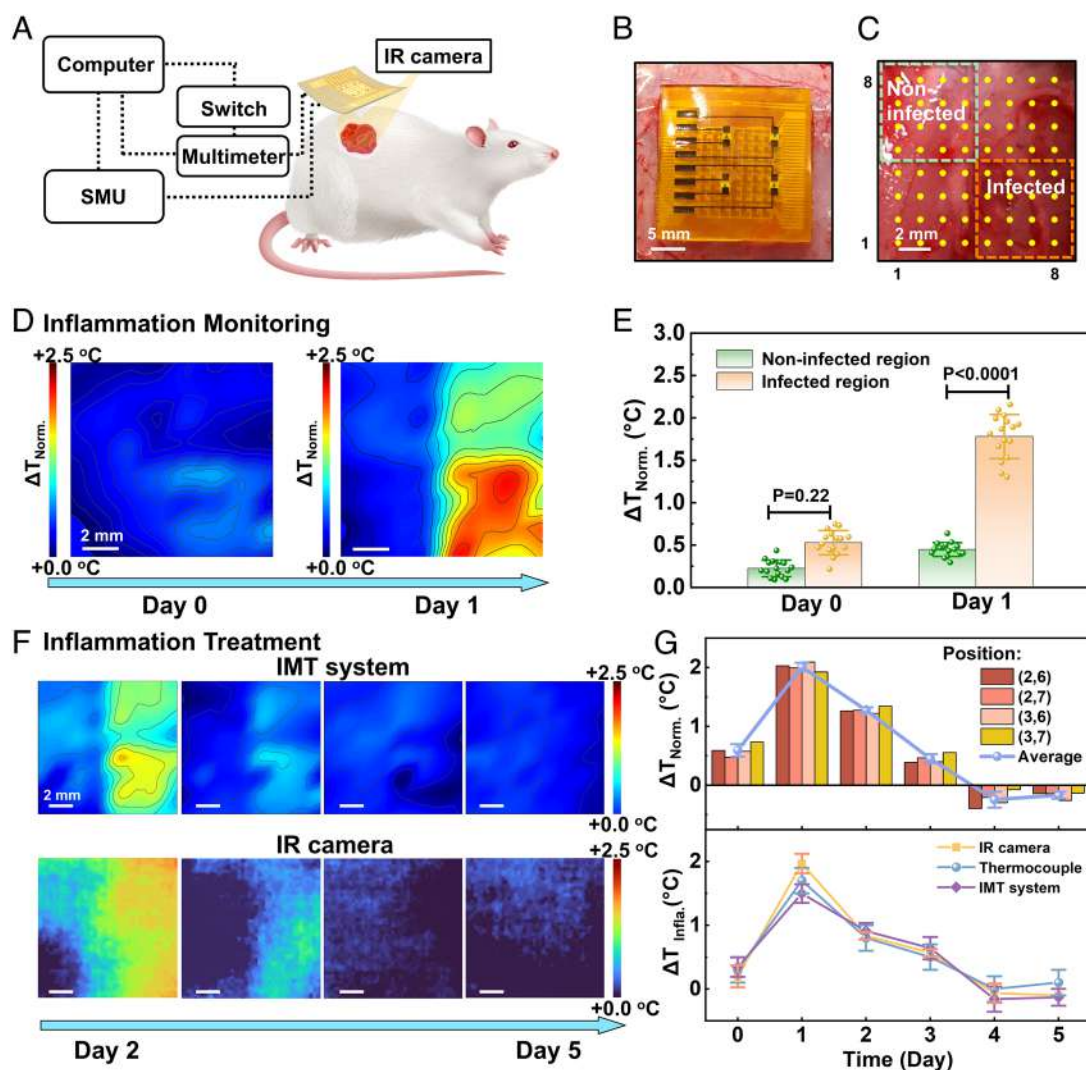


**Fig. 3.** Full-course monitoring and treatment of IMT systems for wound inflammation in animal models. (A) Experimental setup for monitoring and treatment of the wound with localized infection. (B) Photograph of an IMT system attached to the wound. (C) Illustration of temperature sensor channel layout on the wound with infected region (orange frame) and noninfected region (green frame). (D) Temperature distribution across the wound on Day 0 and Day 1 for inflammation localization. (E) Statistic results for identification of localized inflammation. (F) Temperature distribution across the wound after drug release for healing assessment (*Top*) and thermal images captured by IR camera for comparison (*Bottom*). (G) Full-course temperature monitoring (*Top*) and the comparison with commercial sensors (*Bottom*).

CFU mL<sup>-1</sup> of *Staphylococcus aureus* that can rapidly induce the inflammation. The diagonal areas represent noninfected regions (we take the green frame as a comparison). Each unit can be addressed through the index of column and row for following analysis, ranging from (1,1) to (8,8). Detailed information can be found in *SI Appendix, Texts S12 and S13*. After the infection at the specific region, significant pus formation appears after 1 d in the infected region, while the noninfected region remains almost the same on Day 1, as shown in *SI Appendix, Fig. S29*. Fig. 3*D* collects the changes of localized temperatures measured from each sensor unit by bicubic interpolation, before and after the inflammation within 2 d. Here, the values of the temperature change ( $\Delta T_{\text{Norm.}}$ ) can be calculated as the difference between the testing ( $T_{\text{test}}$ ) and reference temperature ( $T_{\text{ref}}$ ) to eliminate the fluctuation of rat body temperature and environment temperature (*SI Appendix, Fig. S29*). Specifically, the entire thermal image presents a relatively uniform temperature distribution before inflammation occurs at Day 0, with an average change of temperature of 0.5 °C through the array. Nevertheless, a noticeable increase of average temperature near 2 °C can be observed on the inflamed region after 1 d (origin frame) compared to the noninfected region (green frame), primarily due to localized inflammation, results of which are well consistent with those of the commercial infrared camera (*SI Appendix, Fig. S30*).

Fig. 3*E* summarizes the multichannel data recorded at infected and noninfected regions, respectively, both of which include temperature changes measured via 16 channels within the first 2 d. As expected, the inflammation results in a dramatic increase of temperature after 1 d with a low *P*-value under 0.0001, which suggests the statistic existence of localized inflammation. As a comparison, the noninfected area at Day 0 offers a higher *P*-value of 0.22, indicating no significant temperature difference during this period. The findings demonstrate that the IMT system can locate the area of inflammation and assess the severity of the inflammation based on local temperature differences.

For the following drug delivery, the IMT system can immediately initiate the treatment process as the feedback in accordance to the monitoring of localized temperature distribution of the wound region. Upon triggering the IR-LED for drug release through the interfacing hydrogel, Fig. 3*F* collects a set of temperature changes (upper) captured by the IMT system from Day 2 to Day 5, consistent with the results captured *via* the commercial infrared camera (bottom). Specifically, the average change of the localized temperature displays a rapid drop within the infected region (orange frame in Fig. 3*C*) from Day 2, followed by a continuous decrease from 2 °C to 0 °C after the recovery at Day 5. These spatial maps of temperature change via the IMT system not only match those of the commercial tool but also provide high-resolution information associated with the inflammation about the profile of the infected regions. Such capability enhances the monitoring effectiveness, allowing for high-precise assessment of the inflammation severity and the subsequent management of the wound healing process.

As the powerful capability of monitoring and treatment, the IMT system can provide closed-loop functionality to cover the entire process that ranges from inflammation monitoring, to mid-term treatment, and to late-stage healing assessment. The *Top* of Fig. 3*G* exhibits the quantitative measurements of temperature changes of four representative sensor units from the infected region as the examples during the full-course process from Day 0 to Day 5. In agreement to the results of Fig. 3*D* and *F*, the data of temperature change increase significantly within 2 d (inflammation stage) and then continuously decrease from Day 1 to Day 3 (mid-term treatment), followed with stable performance of the sensor units that remains unchanged after

Day 4 (recovery stage). In contrast, *SI Appendix, Fig. S31* shows the data of temperature change recorded from other four representative channels in the noninfected area (green frame in Fig. 3*C*), with minor fluctuations during the same period within 5 d, as expectation to no obvious inflammation in such region. For consistency, results of the temperature difference ( $\Delta T_{\text{Infla.}}$ ) of the infected region and noninfected region obtained from the commercial infrared camera and thermocouple, as demonstrated in yellow and blue at the *Bottom* of Fig. 3*G*, are in excellent agreement with those measured by the sensor array of the IMT system. In this context, these results of the device platform suggest great potential as the smart optoelectronic interfaces for wound tissues, with broad utility in both biomedical research and in clinical practice for real-world applications.

**Circuit Designs and Operating Principles for Automatic, Closed-Loop, Wireless IMT Systems.** The intelligent IMT system with functions of inflammation monitoring, wireless data transmission, and automated therapy provides key advantages in daily monitoring scenarios for closed-loop wound management. Fig. 4*A* illustrates the schematic structure of this automatic, closed-loop, and wireless system. The platform consists of the biointerface module (IR-LED array, temperature sensor array, and drug-loaded hydrogel) and a customized flexible circuit module that assembles essential commercial electronic components such as Bluetooth Low Energy System on Chip (BLE SoC), amplifiers, Metal-Oxide-Semiconductor Field-Effect Transistors (MOSFET), and a battery. The laboratory-grade biointerface module, notable for its excellent softness and biocompatibility, is connected to the circuit module via Anisotropic Conductive Films (ACF). The biointerface module provides regional temperature monitoring and heat-triggered drug release, while the circuit module supports signal processing, on-chip feedback, and wireless data transmission. Fig. 4*B* shows the photography of the individual biointerface module, the circuit module, and the assembled system with ACF. The entire system is mounted on the skin as a smart wristband for wound management in Fig. 4*C*. More details in *SI Appendix, Text S14*.

To ensure accurate electrical signal input and output in our program, Fig. 4*D* outlines the design of a sensing and driving circuit scheme composed of an Analog Front End circuit (AFE) and a BLE system to drive the biointerface module. A quarter-bridge Wheatstone bridge configuration converts temperature to voltage value, followed by amplification and collection. The Microcontroller Unit (MCU) processes data and thus makes reactions by virtue of the General Purpose Input/Output (GPIO). This sensing and driving circuit is extended to four channels to allow for separate collection and stimulation of each channel. See the *Materials and Methods* section for more details. The configuration of the Bluetooth chip features 8 Analog-to-Digital Converter (ADC) pins and 20 GPIO pins, indicating the feasibility of expanding the platform for a fully wireless large array by employing digital multiplexing schemes. Additionally, temperature data and the operational states of the IR-LEDs from all channels are wirelessly transmitted to a customized mobile application *via* Bluetooth protocol, allowing for real-time monitoring of inflammation and treatment states.

Fig. 4*E* describes the signal processing and control flowchart of the customized embedded program within the Bluetooth chip for automatic monitoring and treatment of inflammation. The crucial step is the determination of the presence and location of inflammation sites based on predefined conditions including time intervals ( $T_{\text{on}}$  and  $T_{\text{off}}$ , defined as duration time of IR-LED on and off) and threshold temperature that can be defined as the maximum temperature difference between sensors ( $\Delta T_{\text{max}}$ ), which determines the subsequent treatment or not. Wireless data transmission

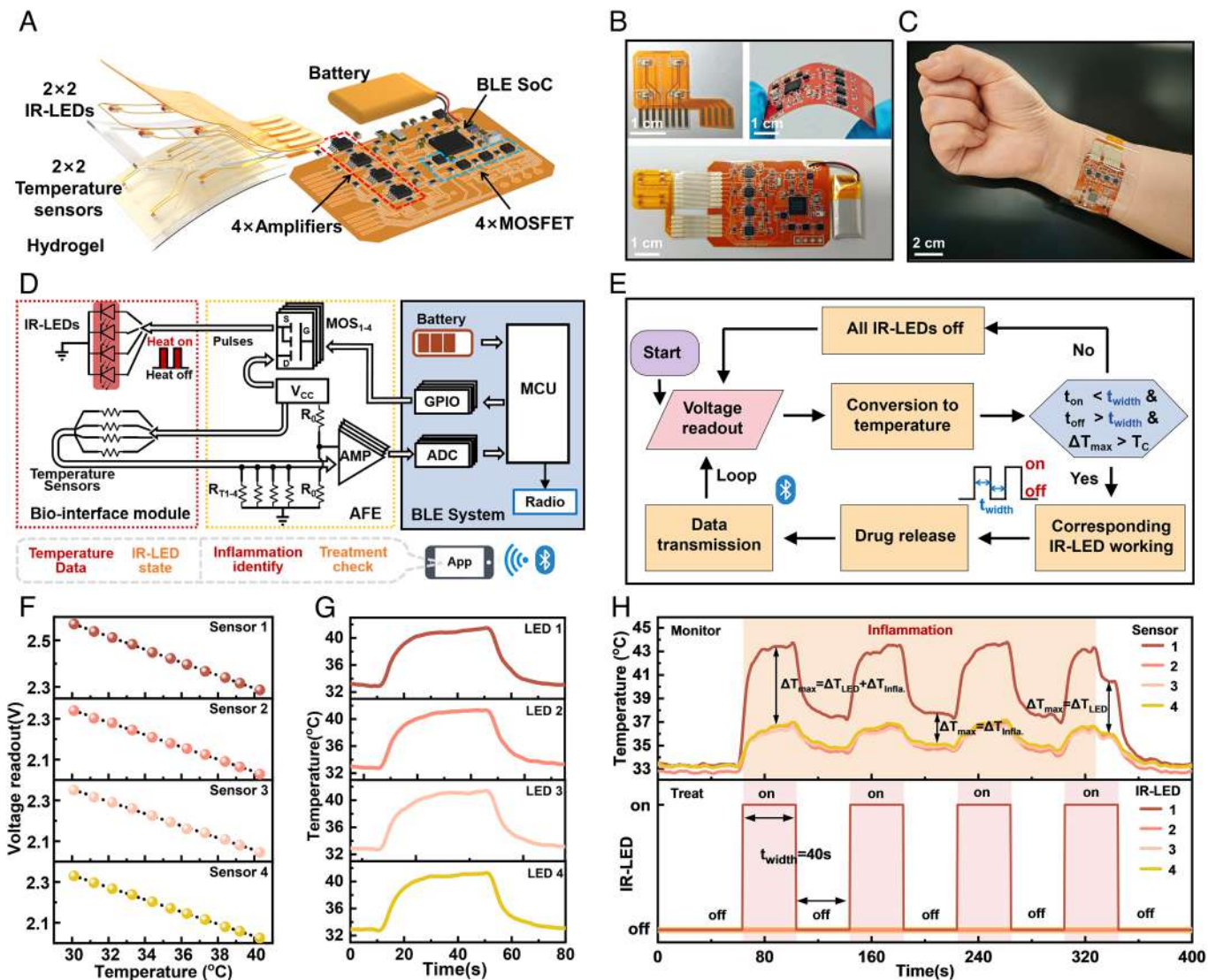


**Fig. 4.** Circuit designs and operating principles for automatic, closed-loop, and wireless IMT systems. (A) Structure illustration of the fully assembled, integrated wireless IMT system showing soft sensing/actuating components, FPCB circuit, and surface-mounted electronic components. (B) Optical image of the individual biointerface module, the circuit module, and the assembled system with ACF. (C) Optical image of the entire IMT system mounted on the skin as a smart wristband for wound management. (D) Schematic illustration of a biointerface module, an AFE circuit, and a BLE system with custom mobile phone application for real-time data readout. (E) Program flow chart for automated monitoring and treatment. (F) Calibration curves of output voltage signal in function of actual temperature. (G) The temperature-time curves of four IR-LEDs operating under pulse mode. (H) Monitoring and treatment process of simulated localized inflammation on artificial skin. Measured temperature data (*Top*) and IR-LED states readout (*Bottom*).

to the mobile application occurs at the final step of each cycle. More details can be found in the *Materials and Methods* section.

Experiments have validated the capability of developed IMT systems for automatic inflammation monitoring, treatment, and wireless data transmission. The raw voltage data from four channels collected by ADC are converted to actual temperature values using linear calibration curves for monitoring, as shown in Fig. 4F. The ADC resolution of 3 mV determines that temperature monitoring resolution can reach as low as 0.1 °C. The temperature-time curves of the four IR-LEDs, which operate under pulse modes, are displayed in Fig. 4G. After being activated, the IR-LEDs increase the temperature from a baseline of 33 °C (typical human epidermal temperature) to over 40 °C (drug release temperature) within 20 s. The temperature then slowly reaches saturation near 43 °C and drops to the initial baseline level within 30 s after switching the IR-LEDs off. For effective heat-triggered therapy and continuous temperature-based inflammation monitoring, the duration and pause of IR-LED heating must exceed the required time for the temperature to rise to drug release level (40 °C) and to cool down (33 °C), respectively. This is to ensure that the IR-LEDs

can maintain the maximum drug release temperature long enough to complete the drug release process and then sufficiently cool down to avoid interfering with the measurement of actual wound temperature.

Fig. 4H demonstrates the monitoring and treatment process of localized inflammation on an artificial skin of PDMS. An 808 nm laser generator can yield a laser spot (3 mm diameter) to simulate the inflammation area right on the site of sensors (here we take Sensor 1# as an example). When the laser is triggered, the temperature readout of Sensor 1# apparently exceeds those of other sensors, thus leading to a maximum temperature difference ( $\Delta T_{\max}$ ) of more than 2 °C between Sensor 1# and the other sensors (2#, 3#, and 4#). Consequently, the system identifies the presence of inflammation at Sensor 1# location and initiates the pulse heating of corresponding IR-LED 1# ( $t_{\text{width}} = 40$  s). In order to decouple the heat between that from IR-LED and from the inflammation, the  $\Delta T_{\max}$  in Fig. 4H corresponds to the measurements of Sensor 1# that include the results both from the IR-LED 1# ( $\Delta T_{\text{LED}}$ ) and from localized inflammation ( $\Delta T_{\text{Infla}}$ ). Once IR-LED 1 is off and thus



the temperature measurements subsequently stabilize, the  $\Delta T_{\max}$  only reflects the heat from the localized inflammation ( $\Delta T_{\text{Infla.}}$ ). In this manner, the  $\Delta T_{\max}$  at this point serves as the key diagnostic indicator to initiate another pulse cycle to IR-LED 1#. The entire process is totally automated, with all data managed through a mobile phone application interface (Movies S1). This advanced IMT system, including the device structure, accompanying circuit design, and embedded program, enables unique capability in inflammation localization and in situ feedback therapy for daily wound care.

**Analysis for the Medical Treatment of the IMT Systems.** Evaluating the therapeutic effects of the IMT systems is of critical importance because they can serve as stable implants for long-term wound healing in ways that create significant functional capabilities (i.e., monitoring and treatments) of relevance to both biomedical research and clinical practices. Fig. 5 shows the histological and immunohistochemical analysis for validations of IMT systems for inflammation suppression. Here, to comprehensively investigate the effect of the IR-LED and hydrogels, the contrast experiments include four groups: 1) the Blank group without the IMT system; 2) the Hydrogel group that only involves the drug-loaded hydrogel patch attached; 3) the IR-LED group that only applies IR-LED illumination on the wound; and 4) the IMT-System group that includes both hydrogel patch and IR-LED. Experimental details can be found in SI Appendix, Text S13. Fig. 5A illustrates optical images of the representative infected wound regions of

the Blank group and IMT-System group. In contrast with the results of the Blank group (Upper in Fig. 5A) displaying obvious signs of moisture and suppuration, particularly during Day 1 to Day 4, the results of the IMT-System group (Bottom in Fig. 5A) reveals that the IMT system essentially suppresses the associated inflammation symptom during the healing process up to Day 5, while the wound in the IMT-System group forms mature scar that suggests more efficient recovery from the inflammation. The results of the Hydrogel group and IR-LED group are similar to those of the Blank group, which shows minor therapeutic effect (SI Appendix, Fig. S32). Fig. 5B summarizes the calculated wound area of the regions over the 6 d, where results of IMT-System group show relatively fast healing process from Day 0 to Day 2 compared to those of the Blank group, primarily due to the rapid drug delivery from the IMT system. These two groups of data eventually approach to a stable level after the treatment process.

Beyond this, Fig. 5C and D provides the assessments of the histopathological structures of tissue slices collected from the infected wounds w/o treatments, by use of hematoxylin-eosin (H&E) and Masson trichrome staining, respectively. More contrast results of the Hydrogel group and IR-LED group are presented in SI Appendix, Figs. S33 and S34. Among the four groups, the results of H&E staining of the IMT-System group (Right in Fig. 5C) reveal significantly less inflammatory cells and more fibroblast migration than those of the other group (Left in Fig. 5C and SI Appendix, Fig. S33), thereby illustrating weakened inflammation level and thus

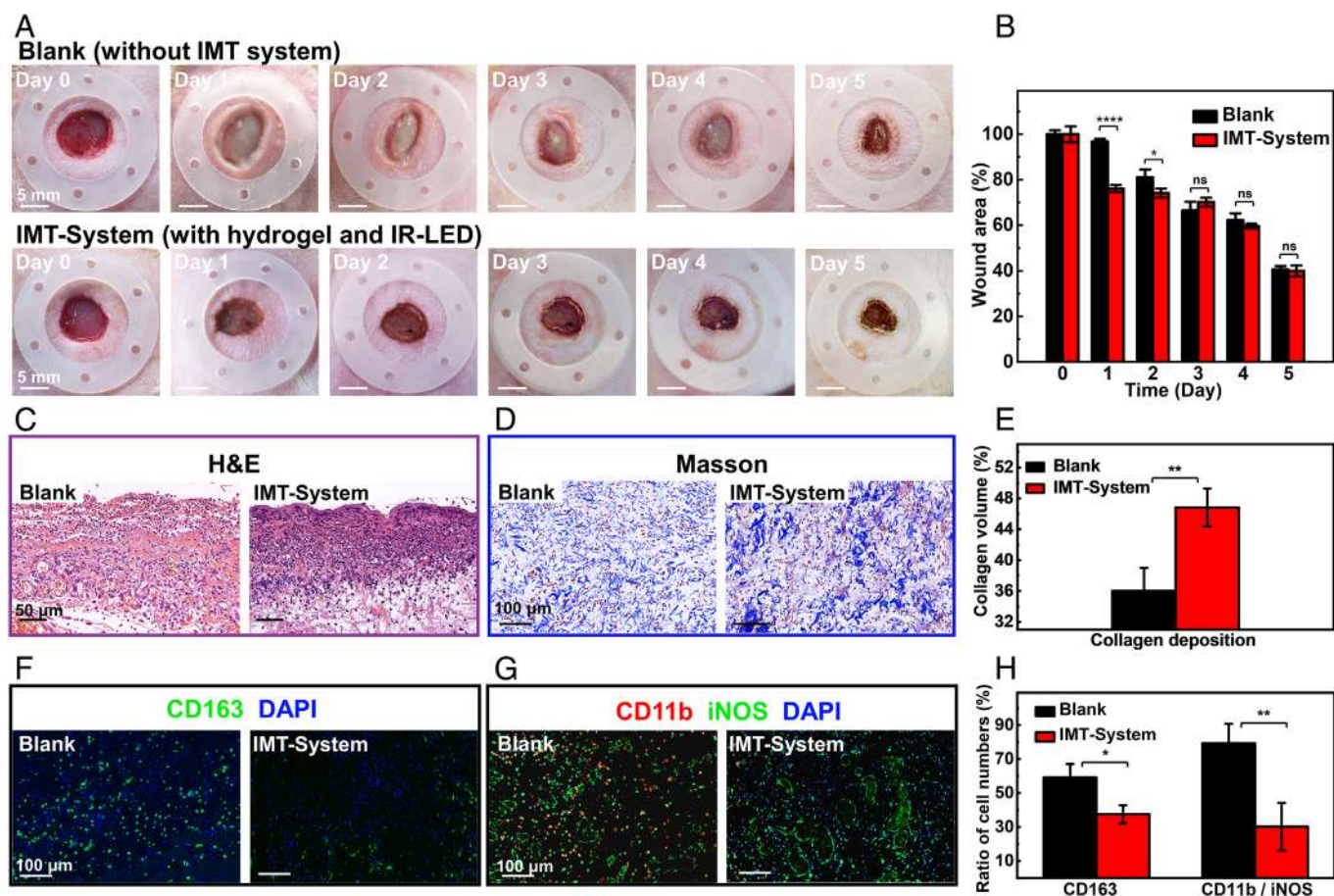


**Fig. 5.** Histological and immunohistochemical analysis for validations of inflammation healing. (A) Images of infected wounds w/o the aid of IMT systems. Obvious signs of moisture and suppuration only appear in the Blank group. (B) Changes of relative wound area. (C) H&E staining and (D) Masson trichrome staining of wound tissues. (E) Statistics of collagen deposition in wound tissues. Higher collagen volume can be captured in the IMT-System group (47%), superior to that of the Blank group (36%). (F) Immunofluorescence staining of CD163 markers. (G) Immunofluorescence staining of M1 cells (CD11b, iNOS). (H) Statistics of the ratio of inflammatory cells. Both the inflammatory factor CD163 and M1 macrophages possess a lower expression level in the IMT-System group. Error bars represent SD ( $n \geq 3$ ). The ns (no significance)  $P > 0.05$ , \* $P < 0.05$ , \*\* $P < 0.01$ , \*\*\* $P < 0.001$ , \*\*\*\* $P < 0.0001$ .

rapid healing process by virtue of IMT systems. In parallel, Fig. 5D and *SI Appendix, Fig. S34*, show the Masson's trichrome staining results, demonstrating that the IMT-System group can offer a higher collagen deposition level with mature recovery of wound tissues. This is consistent with the statistics in Fig. 5E and *SI Appendix, Fig. S34*, which show the collagen volume of the Blank group (36%), Hydrogel group (40%), IR-LED group (36%), and IMT-System group (47%). These findings suggest the aid of IMT systems can enable effective wound healing by delivering drugs, with excellent biocompatibility as stable wound implants.

Evaluation of the immunohistochemical analysis at the cellular level can further assess the capability of IMT systems in inflammation modulation. Fig. 5F and G presents the immunofluorescence staining of various cell markers, as a comparison between the groups. The expression level of the inflammatory factor CD163 in the IMT-System group is significantly lower than those of the other groups (Fig. 5F and *SI Appendix, Fig. S35*), while the M1 macrophages costained by inducible nitric oxide synthase (iNOS) and macrophage marker (CD11b) are observably decreased (Fig. 5G). Overall, the resultant statistics of the proportion of inflammatory cells appear in Fig. 5H and *SI Appendix, Fig. S35*, with results of each ratio of cell numbers (which is defined as the proportion of inflammatory cells in the total cell population within the field of view), indicating that the treatment of the IMT system can effectively suppress inflammation.

## Discussion

In summary, the results presented here establish a design of material, device structure, and a scheme of system integration for the bioelectronic interface with capabilities of inflammation localization and targeted treatment for closed-loop wound management. Systematic device characterization reveals the thermal, electronic, and antibacterial performance of sensors/actuators, where the platform consists of the temperature sensor array, the IR-LED array, and the drug-loaded hydrogel for treatments. Detailed simulations and experiments highlight the capability of thermal imaging for the use of a wide range of targets that includes artificial skins, live animal models, and the human body. Furthermore, effective utility on biologic entities is demonstrated by the following *in vivo* experiments, where integration of diagnosis and treatment is implemented and histological recovery is observed. To offer a more feasible, accessible application for clinical usage, the advanced version incorporates carefully designed electronic hardware for automatic manipulation and wireless data transmission. These findings potentially form the unique approach to identify and manage the wound inflammation in the dimensions of both time and space. Ongoing work seeks to establish a more powerful material system as the bioelectronic interface with exceptional biological repair functions. For further application, these same strategies can hopefully extend to implementable electronic/optoelectronic device platforms as helpful tools for research of organ and nervous systems.

## Materials and Methods

**Fabrication of the Amorphous Silicon Temperature Sensor Array.** The fabrication began with the cleaned glass substrates with a 10:1 mixture (base: curing agent) of PDMS (Dow Corning) spin-coated (3,000 rpm, 30 s). A transparent PI film with a thickness of 12  $\mu\text{m}$  (Chenfan) was cut to the appropriate size and carefully attached to the PDMS-coated glass, followed by curing at room temperature for over 24 h. Amorphous silicon (300 nm) was then deposited using RF magnetron sputtering (DE500, DE Technology). Photolithography (MA6, SUSS) with photoresist Az5214 and reactive ion etching (T2, Trion) defined the pattern of the amorphous silicon, forming the layout of the device array. A first

layer of metal interconnects (Cr/Au 5/100 nm) was deposited by magnetron sputtering, patterned by photolithography and etching. SU-8 2002 (Microchem) was then spin-coated (3,000 rpm, 30 s for 2  $\mu\text{m}$ ) as an insulating intermediate layer with via holes defined by subsequent photolithography. A second layer of metal interconnects (Cr/Au 10/200 nm) was deposited by magnetron sputtering, patterned by photolithography and etching. Finally, SU-8 2005 (Microchem) was spin-coated (3,000 rpm, 30 s for 5  $\mu\text{m}$ ) as a top protective layer, with electrode via holes created by photolithography. The completed device was carefully peeled from the glass substrate, finalizing the fabrication of the flexible amorphous silicon temperature sensor array.

**Drugs and Fabrication of the Drug-Loaded Hydrogel.** Amoxicillin, a type of penicillin, serves as the treatment drug for wound inflammation. To ensure the effectiveness and safety of the treatment, the mass fraction of the drug in the hydrogel is 0.25% in our case. For the fabrication of drug-loaded hydrogels, *SI Appendix, Fig. S1*, illustrates the detailed preparation process for the hydrogel composition. To begin with, gelatin granules (Sinoreagent) were mixed with deionized water in a mass ratio of 3:7 at 100  $^{\circ}\text{C}$ , as the basis for hydrogel materials, followed with adding 0.25 wt% of amoxicillin powder dissolved in the liquid solutions at 50  $^{\circ}\text{C}$ . The physical cross-linking in the customized mold at 4  $^{\circ}\text{C}$  overnight can form the 200  $\mu\text{m}$  thick drug-loaded hydrogel.

**Preparation of the IR-LED Array Layer.** Custom metal interconnect wiring was designed on a Cu/PI/Cu substrate (18/25/18  $\mu\text{m}$ ) provided by JLC Technology Group. IR-LEDs (Hong Guang) were attached to the substrate using Sn/Bi solder paste (HIROSAKI) by reflow soldering. To compensate for the thickness of the IR-LEDs, a custom mold by 3D printing (Raise3D) was used to shape 20:1 PDMS or silicone into a 1 mm thick, centrally hollowed-out soft film, which was then applied to the substrate.

**Remote Wireless Circuit Design and Automated Embedded Program Construction.** The flexible circuit comprised a BLE SoC (nRF 52832, Nordic), a Low-Dropout regulator (TPS7A37, Texas Instruments), four differential amplifiers (INA333, Texas Instruments), four MOSFETs (CSD15571Q2, Texas Instruments), a 2.4 GHz mini antenna (2450AT18A100), and a lithium-ion battery (60 mAh, JieXun). Other components including resistors and capacitors were from Chuangli. The BLE module and instrumentation amplifiers were powered directly by the lithium-ion battery with a Low-Dropout regulator to adjust VCC to 3 V. Each temperature sensor was formed as a Wheatstone bridge together with three resistors on the flexible circuit, and the voltage difference was measured using instrumentation amplifiers. The resistance of the bridge arms, the gain of the amplifier, and the reference voltage were all adjustable to ensure the amplifier's output voltage within the measuring range of the ADC. The four MOSFETs were utilized for switching on/off state of IR-LEDs by high/low output of four GPIOs. Each IR-LED was equipped with a resistor connected in series to limit the maximum operating current. The assembled Bluetooth circuit can achieve remote wireless data transmission of more than ten meters. The embedded program was constructed in Keil  $\mu\text{Vision}$  IDE and Arduino IDE, which fit to the microcontroller unit with the ARM Cortex-M4 processor.

**FEA Simulation and Data Process.** Data were presented with average values and SD, unless noted in the figure caption. Linear regression analysis of measured temperature sensor data was used to generate temperature calibration curves for all sensors via ORIGIN. The two-sample t test was done in ORIGIN. The cubic interpolated temperature distribution was calculated and displayed with MATLAB. All simulations of heat diffusion and heat conductance were conducted in COMSOL Multiphysics<sup>®</sup>. All data plotting was done in ORIGIN.

**Ethics Approval.** All human subject studies were approved by the Ethics Committee of Zhongshan Hospital, Fudan University. ID: Y2021073. Informed consent was obtained from all participants involved in this entire study. All animal studies were conducted according to the experimental practices and standards approved by the Animal Welfare and Research Ethics Committee at Fudan University (Approval ID: 202312020S) and Shanghai Yishang Biotechnology Co., Ltd (Approval ID: 2024-Rat-203).

More comprehensive details of fabrication processes, device structures, performance characteristics, and closed-loop strategies appear in *SI Appendix*. Operation of the *in vivo* test of the IMT systems, designs of the circuit/program, and pathological analysis of wound tissue are also in *SI Appendix*. The original

data of this paper are deposited in the Fudan University Social Science Data Repository (<https://dvn.fudan.edu.cn/dataset.xhtml?persistentId=hdl:11521/172VZP>). The associated protocols, code, and materials that support the findings of this study are included in the article and/or *SI Appendix*.

**Data, Materials, and Software Availability.** All data are included in the manuscript and/or [supporting information](#). The source data for the figures in this study are available in Fudan University Social Science Data Repository (<hdl:11521/172VZP>) (61).

**ACKNOWLEDGMENTS.** This work is supported by the STI 2030-Major Project (2022ZD0209900), the National Natural Science Foundation of China (62204057, 62304044, and 82304124), Science and Technology Commission of Shanghai Municipality (22ZR1406400), and Lingang Laboratory (LG-QS-202202-02), and we appreciate the support by State Key Laboratory of Integrated Chips and Systems (SKLICS-Z202306), Shanghai Municipal Science and Technology Major Project (2018SHZDX01), State Key Laboratory of Medical Neurobiology and Ministry of Education Frontiers Center for Brain Science, the young scientist project of Ministry of Education innovation platform, and the China Postdoctoral Science Foundation (2023M730712). Part of the experimental work was carried out in Zhongshan Hospital, Shanghai Yishang Biotechnology Co., Ltd, and Fudan Nanofabrication Laboratory.

1. M. Farahani, A. Shafiee, Wound healing: From passive to smart dressings. *Adv. Healthc. Mater.* **10**, 2100477 (2021).
2. V. Kalidasan *et al.*, Wirelessly operated bioelectronic sutures for the monitoring of deep surgical wounds. *Nat. Biomed. Eng.* **5**, 1217–1227 (2021).
3. G. H. Lee *et al.*, Multifunctional materials for implantable and wearable photonic healthcare devices. *Nat. Rev. Mater.* **5**, 149–165 (2020).
4. Y. Jiang *et al.*, Wireless, closed-loop, smart bandage with integrated sensors and stimulators for advanced wound care and accelerated healing. *Nat. Biotechnol.* **41**, 652–662 (2023).
5. S. Matoori, A. Veves, D. J. Mooney, Advanced bandages for diabetic wound healing. *Sci. Transl. Med.* **13**, eabe4839 (2021).
6. F. A. R. Mota, M. L. C. Passos, J. L. M. Santos, M. Saraiva, Comparative analysis of electrochemical and optical sensors for detection of chronic wounds biomarkers: A review. *Biosens. Bioelectron.* **251**, 116095 (2024).
7. C. Wang *et al.*, Wound management materials and technologies from bench to bedside and beyond. *Nat. Rev. Mater.* **9**, 550–566 (2024). [10.1038/s41578-024-00693-y](https://doi.org/10.1038/s41578-024-00693-y).
8. N. T. Garland *et al.*, A miniaturized, battery-free, wireless wound monitor that predicts wound closure rate early. *Adv. Healthc. Mater.* **12**, 2301280 (2023).
9. B. Mirani *et al.*, An advanced multifunctional hydrogel-based dressing for wound monitoring and drug delivery. *Adv. Healthc. Mater.* **6**, 1700718 (2017).
10. Z. Xiong *et al.*, A wireless and battery-free wound infection sensor based on DNA hydrogel. *Sci. Adv.* **7**, eabj1617 (2021).
11. S. Nakata, T. Arie, S. Akita, K. Takei, Wearable, flexible, and multifunctional healthcare device with an ISFET chemical sensor for simultaneous sweat pH and skin temperature monitoring. *ACS Sens.* **2**, 443–448 (2017).
12. Q. Pang *et al.*, Smart flexible electronics-integrated wound dressing for real-time monitoring and on-demand treatment of infected wounds. *Adv. Sci.* **7**, 1902673 (2020).
13. J. Xiao, Z. Zhou, G. Zhong, T. Xu, X. Zhang, Self-sterilizing microneedle sensing patches for machine learning-enabled wound pH visual monitoring. *Adv. Funct. Mater.* **34**, 2315067 (2024).
14. C. Zhang *et al.*, Wireless, smart hemostasis device with all-soft sensing system for quantitative and real-time pressure evaluation. *Adv. Sci.* **10**, 2303418 (2023).
15. Z. Y. Ge *et al.*, Wireless and closed-loop smart dressing for exudate management and on-demand treatment of chronic wounds. *Adv. Mater.* **35**, 2304005 (2023).
16. E. Shirzaei Sani *et al.*, A stretchable wireless wearable bioelectronic system for multiplexed monitoring and combination treatment of infected chronic wounds. *Sci. Adv.* **9**, ead7388 (2023).
17. J. W. Song *et al.*, Bioresorbable, wireless, and battery-free system for electrotherapy and impedance sensing at wound sites. *Sci. Adv.* **9**, eade4687 (2023).
18. N. Tang *et al.*, Highly efficient self-healing multifunctional dressing with antibacterial activity for sutureless wound closure and infected wound monitoring. *Adv. Mater.* **34**, 2106842 (2022).
19. G. Xu *et al.*, Battery-free and wireless smart wound dressing for wound infection monitoring and electrically controlled on-demand drug delivery. *Adv. Funct. Mater.* **31**, 2100852 (2021).
20. S. M. Yang *et al.*, Soft, wireless electronic dressing system for wound analysis and biophysical therapy. *Nano Today* **47**, 101685 (2022).
21. M. Han *et al.*, Catheter-integrated soft multilayer electronic arrays for multiplexed sensing and actuation during cardiac surgery. *Nat. Biomed. Eng.* **4**, 997–1009 (2020).
22. J. Li *et al.*, Conductively coupled flexible silicon electronic systems for chronic neural electrophysiology. *Proc. Natl. Acad. Sci. U.S.A.* **115**, E9542–E9549 (2018).
23. E. Song *et al.*, Miniaturized electromechanical devices for the characterization of the biomechanics of deep tissue. *Nat. Biomed. Eng.* **5**, 759–771 (2021).
24. S. E. Gardner *et al.*, A tool to assess clinical signs and symptoms of localized infection in chronic wounds: Development and reliability. *Ostomy Wound Manag.* **47**, 40–47 (2001).
25. A. A. Lombardi *et al.*, Mitochondrial calcium exchange links metabolism with the epigenome to control cellular differentiation. *Nat. Commun.* **10**, 4509 (2019).
26. D. Wang, Y. Liu, Y. R. Zhao, J. L. Zhou, Low dose of lipopolysaccharide pretreatment can alleviate the inflammatory response in wound infection mouse model. *Chin. J. Traumatol.* **19**, 193–198 (2016).
27. B. B. Lowell, B. M. Spiegelman, Towards a molecular understanding of adaptive thermogenesis. *Nature* **404**, 652–660 (2000).

Author affiliations: <sup>a</sup>Department of Materials Science and Institute of Optoelectronics, Shanghai Frontiers Science Research Base of Intelligent Optoelectronics and Perception, Fudan University, Shanghai 200438, China; <sup>b</sup>State Key Laboratory of Integrated Chips and Systems, Fudan University, Shanghai 200438, China; <sup>c</sup>International Institute for Intelligent Nanorobots and Nanosystems, Center for Neural Regulation and Brain-Computer Interface Research, Fudan University, Shanghai 200438, China; <sup>d</sup>Yiwu Research Institute of Fudan University, Yiwu, Zhejiang 322000, China; <sup>e</sup>Institute of Agro-food Technology, Jilin Academy of Agricultural Sciences (Northeast Agricultural Research Center of China), Changchun 130033, China; <sup>f</sup>Department of Ophthalmology, Tongji Hospital, School of Medicine, Tongji University, Shanghai 200065, China; <sup>g</sup>Sichuan Provincial Key Laboratory for Human Disease Gene Study and the Center for Medical Genetics, School of Life Science and Technology, University of Electronic Science and Technology of China, Chengdu 611731, China; <sup>h</sup>Department of Nutrition and Food Hygiene, School of Public Health, Institute of Nutrition, Fudan University, Shanghai 200030, China; <sup>i</sup>State Key Laboratory of Functional Materials for Informatics, Shanghai Institute of Microsystem and Information Technology, Chinese Academy of Sciences, Shanghai 200050, China; <sup>j</sup>Department of Electronic Engineering, Beijing National Research Center for Information Science and Technology, Tsinghua University, Beijing 100084, China; and <sup>k</sup>Institute for Precision Medicine, Center for Flexible Electronics Technology, IDG/McGovern Institute for Brain Research, Tsinghua University, Beijing 100084, China

Author contributions: J.L., N.H., Y.M., and E.S. designed research; J.L., Z.L., M.S., Y.S., and C.L. performed research; L.L. and X.S. contributed new reagents/analytic tools; J.L., Y.L., B.H., Y.M., and E.S. analyzed data; and J.L., L.Z., X.W., Z.W., C.Y., M.W., L.T., Z.D., Y.M., and E.S. wrote the paper.

The authors declare no competing interest.

This article is a PNAS Direct Submission.

28. Y. F. Zhong *et al.*, The importance of temperature monitoring in predicting wound healing. *J. Wound Care* **32**, lxxxvii–xcvi (2023).
29. R. Derwin, D. Patton, H. Strapp, Z. Moore, The effect of inflammation management on pH, temperature, and bacterial burden. *Int. Wound J.* **20**, 1118–1129 (2023).
30. G. Gethin *et al.*, What is the “normal” wound bed temperature? A scoping review and new hypothesis. *Wound Repair Regen.* **29**, 843–847 (2021).
31. K. Sim *et al.*, An epicardial bioelectronic patch made from soft rubbery materials and capable of spatiotemporal mapping of electrophysiological activity. *Nat. Electron.* **3**, 775–784 (2020).
32. E. Song, J. Li, S. M. Won, W. Bai, J. A. Rogers, Materials for flexible bioelectronic systems as chronic neural interfaces. *Nat. Mater.* **19**, 590–603 (2020).
33. S. M. Won *et al.*, Recent advances in materials, devices, and systems for neural interfaces. *Adv. Mater.* **30**, 1800534 (2018).
34. R. C. Webb *et al.*, Ultrathin conformal devices for precise and continuous thermal characterization of human skin. *Nat. Mater.* **12**, 938–944 (2013).
35. D. H. Kim *et al.*, Thin, flexible sensors and actuators as ‘instrumented’ surgical sutures for targeted wound monitoring and therapy. *Small* **8**, 3263–3268 (2012).
36. M. Sharifuzzaman *et al.*, Smart bandage with integrated multifunctional sensors based on MXene-functionalized porous graphene scaffold for chronic wound care management. *Biosens. Bioelectron.* **169**, 112637 (2020).
37. M. Sang *et al.*, Ultrahigh sensitive Au-doped silicon nanomembrane based wearable sensor arrays for continuous skin temperature monitoring with high precision. *Adv. Mater.* **34**, 2105865 (2022).
38. C. Wang *et al.*, Advanced carbon for flexible and wearable electronics. *Adv. Mater.* **31**, 1801072 (2019).
39. J. J. Kim, G. R. Stafford, C. Beauchamp, S. A. Kim, Development of a dental implantable temperature sensor for real-time diagnosis of infectious disease. *Sensors* **20**, 3953 (2020).
40. M. Gong *et al.*, Flexible breathable nanomesh electronic devices for on-demand therapy. *Adv. Funct. Mater.* **29**, 1902127 (2019).
41. J. Zhang *et al.*, Mechanically robust, flexible, fast responding temperature sensor and high-resolution array with ionically conductive double cross-linked hydrogel. *Adv. Funct. Mater.* **34**, 2314433 (2024).
42. J. Shin *et al.*, Sensitive wearable temperature sensor with seamless monolithic integration. *Adv. Mater.* **32**, 1905527 (2020).
43. H. Ryu *et al.*, Materials and device designs for wireless monitoring of temperature and thermal transport properties of wound beds during healing. *Adv. Healthc. Mater.* **13**, 2302797 (2024).
44. T. Yokota *et al.*, Ultraflexible, large-area, physiological temperature sensors for multipoint measurements. *Proc. Natl. Acad. Sci. U.S.A.* **112**, 14533–14538 (2015).
45. X. Ren *et al.*, A low-operating-power and flexible active-matrix organic-transistor temperature-sensor array. *Adv. Mater.* **28**, 4832–4838 (2016).
46. P. Bainbridge *et al.*, Comparing test methods for moisture-vapor transmission rate (MVTR) for vascular access transparent semipermeable dressings. *J. Vascular Access* **24**, 1000–1007 (2023).
47. R. Xu *et al.*, Novel bilayer wound dressing composed of silicone rubber with particular micropores enhanced wound re-epithelialization and contraction. *Biomaterials* **40**, 1–11 (2015).
48. C. Dagdeviren *et al.*, Conformal piezoelectric systems for clinical and experimental characterization of soft tissue biomechanics. *Nat. Mater.* **14**, 728–736 (2015).
49. M. O. G. Nayeem *et al.*, All-nanofiber-based, ultrasensitive, gas-permeable mechanoacoustic sensors for continuous long-term heart monitoring. *Proc. Natl. Acad. Sci. U.S.A.* **117**, 7063–7070 (2020).
50. N. Tang *et al.*, Wearable sensors and systems for wound healing-related pH and temperature detection. *Micromachines* **12**, 430 (2021).
51. J. L. Ramirez-Garcialuna, R. Bartlett, J. E. Arriaga-Caballero, R. D. J. Fraser, G. Saiko, Infrared thermography in wound care, surgery, and sports medicine: A review. *Front. Physiol.* **13**, 838528 (2022).
52. J. S. Park, Flexible platinum temperature sensor embedded in polyimide (PI) films for curved surface temperature monitoring applications: Skin temperature of human body. *Sens. Mater.* **29**, 1275–1283 (2017).
53. C. Yu, Z. Wang, H. Yu, H. Jiang, A stretchable temperature sensor based on elastically buckled thin film devices on elastomeric substrates. *Appl. Phys. Lett.* **95**, 141912 (2009).

54. S. R. Krishnan *et al.*, Epidermal electronics for noninvasive, wireless, quantitative assessment of ventricular shunt function in patients with hydrocephalus. *Sci. Transl. Med.* **10**, eaat8437 (2018).
55. H. Fang *et al.*, Ultrathin, transferred layers of thermally grown silicon dioxide as biofluid barriers for biointegrated flexible electronic systems. *Proc. Natl. Acad. Sci. U.S.A.* **113**, 11682–11687 (2016).
56. C. Zhu *et al.*, Stretchable temperature-sensing circuits with strain suppression based on carbon nanotube transistors. *Nat. Electron.* **1**, 183–190 (2018).
57. N. A. Martin, S. Falder, A review of the evidence for threshold of burn injury. *Burn* **43**, 1624–1639 (2017).
58. A. R. Moritz, F. C. Henriques, Studies of thermal injury: II. The relative importance of time and surface temperature in the causation of cutaneous burns. *Am. J. Pathol.* **23**, 695–720 (1947).
59. R. W. Korsmeyer *et al.*, Mechanisms of solute release from porous hydrophilic polymers. *Int. J. Pharm.* **15**, 25–35 (1983).
60. P. L. Ritger, N. A. Peppas, A simple equation for description of solute release II. Fickian and anomalous release from swellable devices. *J. Control. Rel.* **5**, 37–42 (1987).
61. J. Liu, Data from "Flexible bioelectronic systems with large-scale temperature sensor arrays for monitoring and treatments of localized wound inflammation." Fudan University Social Science Data Repository. <https://dvn.fudan.edu.cn/dataset.xhtml?persistentId=hdl:11521/172VZP>. Deposited 3 October 2024.

## **Supporting Information for**

## **Flexible bioelectronic systems with large-scale temperature sensor array for monitoring and treatments of localized wound inflammation**

Junhan Liu, Zhongzheng Li, Mubai Sun, Lianjie Zhou, Xiaojun Wu, Yifei Lu, Yuting Shao, Chang Liu, Ningge Huang, Bofan Hu, Zhongyuan Wu, Chunyu You, Lizhu Li, Ming Wang, Ling Tao, Zengfeng Di, Xing Sheng, Yongfeng Mei\*, Enming Song\*

Yongfeng Mei\*, Enming Song\*

Email: yfm@fudan.edu.cn, sem@fudan.edu.cn

### **This PDF file includes:**

- Supporting Text S1 to S14
- Figures S1 to S35
- Table S1
- Legends for Movies S1
- Legends for Software S1
- SI References

### **Other supporting materials for this manuscript include the following:**

- Movies S1
- Software S1

## Supporting Information Text

**Text S1. Fabrication of the amorphous silicon temperature sensor array:** The glass substrates were ultrasonically cleaned sequentially with acetone, ethanol, and deionized water. 10:1 mixture (base: curing agent) of PDMS (Dow Corning) was prepared, stirred in one direction for 3 minutes, and then placed in a vacuum oven for over 30 minutes until all bubbles disappeared. The mixture was then spin-coated onto the glass substrates (3000 rpm, 30 seconds) and allowed to settle in the vacuum oven for another 30 minutes. A transparent PI film with thickness of 12  $\mu\text{m}$  (Chenfan) was cut to the appropriate size and carefully attached to the PDMS-coated glass, followed by curing at room temperature for over 24 hours. The surface of the PI film should be cleaned with acetone and deionized water to remove oils and small particles. Amorphous silicon (300 nm) was then deposited using RF magnetron sputtering (DE500, DE Technology), with base vacuum at 5E-7 and 1E-6 Torr and argon gas flow pressure at 2 mTorr, using RF power mode with power output of 130 W. The resistivity of silicon target (N type, RDMICRO) is 0.9-1 $\Omega$ ·cm. Here, multiple times of sputtering deposition can effectively prevent high substrate temperature that would cause delamination of materials, at a deposition rate of 0.4 nm/second for our case. Photolithography (MA6, SUSS) with photoresist Az5214 and reactive ion etching (T2, Trion) defined the pattern of the amorphous silicon, forming the layout of the device array. A first layer of metal interconnects (Cr/Au 5/100 nm) was deposited by magnetron sputtering, patterned by photolithography and etching. SU-8 2002 (Microchem) was then spin-coated (3000 rpm, 30 seconds for 2  $\mu\text{m}$ ) as an insulating intermediate layer with via holes defined by subsequent photolithography. A second layer of metal interconnects (Cr/Au 10/200 nm) was deposited by magnetron sputtering, patterned by photolithography and etching. Finally, SU-8 2005 (Microchem) was spin-coated (3000 rpm, 30 seconds for 5  $\mu\text{m}$ ) as a top protective layer, with electrode via holes created by photolithography. The completed device was carefully peeled from the glass substrate, finalizing the fabrication of the flexible amorphous silicon temperature sensor array.

**Text S2. Drugs and fabrication of the drug-loaded hydrogel:** Amoxicillin, a type of penicillin, serves as the treatment drug of wound inflammation, which can offer broad-spectrum antibacterial activity against wound infections, including *Streptococcus hemolyticus*, *Staphylococcus*, and *Escherichia coli* (1-3). To ensure the effectiveness and safety of the treatment, the mass fraction of the drug in the hydrogel is 0.25% in our case, also consistent with the results of previous publications for wound inflammation treatments (4,5). For the fabrication of drug-loaded hydrogels, *SI Appendix*, Figure S1 illustrates the detailed preparation process for the hydrogel composition. To begin with, gelatin granules (Sinoreagent) were mixed with deionized water in a mass ratio of 3:7 at 100  $^{\circ}\text{C}$ , as the basis for hydrogel materials, followed with adding 0.25 wt% of amoxicillin powder dissolved in the liquid solutions at 50  $^{\circ}\text{C}$ . The physical cross-linking in the customized mould at 4  $^{\circ}\text{C}$  overnight can form the 200  $\mu\text{m}$  thick drug-loaded hydrogel. As a comparison, such similar approaches for preparation methods are also widely used for hydrogel-based wearable platforms (6-8).

**Text S3. Preparation of the IR-LED array layer:** Custom metal interconnect wiring was designed on a Cu/PI/Cu substrate (18/25/18  $\mu\text{m}$ ) provided by JLC Technology Group. IR-LEDs (Hong Guang) were attached to the substrate using Sn/Bi solder paste (HIROSAKI) by reflow soldering. To compensate for the thickness of the IR-LEDs, a custom mold by 3D printing (Raise3D) was used to shape 20:1 PDMS or silicone into a 1 mm thick, centrally hollowed-out soft film, which was then applied to the substrate.

**Text S4. Assembly and Wiring of the IMT System:** A mold for the IMT system was formed using 3D printing, into which silicone was poured and then cured to form the encapsulating shell. The drug-loaded hydrogel, temperature sensor array layer, and IR-LED array layer were stacked from bottom to top, with the adhesion between layers relying on the cohesive properties of the hydrogel and PDMS/silicone. All connections were made using anisotropic conductive film linked to a PCB adapter board that connected to measurement equipment.

**Text S5. Electrical Characterization of Temperature Sensors:** The I-V curves of the amorphous silicon temperature sensors were measured using a probe station and a semiconductor analyzer (Keithley 4200A). The temperature-resistance calibration involved placing the device on a hotplate, with temperature data taken from a thermocouple (UNI-T UT320A) placed on the surface of the hotplate, and resistance readings directly obtained from a digital multimeter (Keithley 2100). Dynamic testing was conducted by a cup of cold water and warm water. The PXI-2530B Multiplexer Switch Module was used for channel switching. Underneath a 10:1 PDMS film, strip-shaped copper wire resistors and point-shaped IR-LEDs served as simulated heat sources, with a source meter (NGI N2600) supplying current to these heat sources.

**Text S6. FEA Simulation and Data Process:** Data were presented with average values and SD, unless noted in the figure caption. Linear regression analysis of measured temperature sensor data was used to generate temperature calibration curves for all sensors via ORIGIN. The two-sample t-test was done in ORIGIN. The cubic interpolated temperature distribution was calculated and displayed with MATLAB. All simulations of heat diffusion and heat conductance (9) were conducted in COMSOL Multiphysics®. All data plotting was done in ORIGIN.

**Text S7: Calibration of the temperature sensor array:** The electrical resistance values of each sensor were measured at different constant temperatures (30 °C and 45 °C for our case as an example, respectively) in the constant-temperature ovens.  $R$  can approximately equal to the average value and the TCR is considered as constant (10,11). Thus, we calculated the each TCR value based on Equation S1.

$$\text{TCR} = \frac{1}{R} \cdot \frac{dR}{dT} = \frac{R_2 - R_1}{\frac{1}{2}(R_2 + R_1)(T_2 - T_1)} \quad \text{Eq. (S1)}$$

where  $R_2$  and  $T_2$  corresponds to higher-temperature condition (at 45 °C); and  $R_1$  and  $T_1$  stands for lower-temperature condition (at 30 °C), respectively. In this context, the measured temperatures (in range of 30-45 °C) can be determined using the TCR of each sensor, via the following Equation S2:

$$T_{\text{measured}} - T_1 = \frac{R_{\text{measured}} - R_1}{\frac{1}{2}(R_{\text{measured}} + R_1) \cdot \text{TCR}} \quad \text{Eq. (S2)}$$

where  $R_{\text{measured}}$  stands for the electrical resistance of each temperature sensor unit. In this manner, the measurement results of temperature (here refers to  $T_{\text{measured}}$ ) can be determined based on the above calculation. Consistent with previous literatures, these calibration method for temperature sensors have been also widely studied in other reports (10,12,13).

**Text S8. Exposure tests:** For the test within biofluids, we prepared the phosphate buffered saline (PBS, 1X) solution with glucose contents (10 mM/L), serving as the simulated wound fluid (SWF) at constant-temperature ovens at 37 °C and 96 °C. Furthermore, the detailed experiment result can be found in the *SI Appendix*, Figures S16 and S17.

**Text S9. Mechanism and kinetics of drug release:** As the temperature increases with IR-LED at on-state, the conformation of gelatin chains transforms from triple helices to coil, resulting in the melting of the gel and subsequent drug release (*SI Appendix*, Figure S22a-d), with the conversion from gel-state to a sol-state (14-16). For the measurements of drug release kinetics, a group of hydrogel samples (1 cm diameter, 1 mm thick) that each incorporates constant concentration of amoxicillin, serve as the drug-loaded hydrogel immersed into PBS solution at the triggering temperature (40 °C). The drug concentration can be determined using liquid chromatography-mass spectrometry (LC-MS) method. The red equation in *SI Appendix*, Figure S22e can theoretically describe the relationship between the drug release amount and time based on the Korsmeyer–Peppas (K-P) model (17,18) with fitting values of kinetic constant  $k$  and release exponent  $n$  are 3.78 and 2.45, consistent with the ranges of previous publications (19-22). Low temperatures such as 33 °C can yield much lower drug release concentration compared to

that under the triggering temperature of 40 °C after sufficiently long time (~100 times lower), indicating that the drug contents can be effectively limited within the hydrogel (*SI Appendix*, Figure S22f).

**Text S10. Characterization of Heat-Triggered Drug Release from IR-LED and Drug-Loaded Hydrogel:** A source meter supplied working current to the IR-LEDs in a constant current mode, while the temperature of the IR-LEDs was monitored using an infrared camera (Seek Thermal). The drug-loaded hydrogel was cut into circular disks with a diameter of 2 cm and placed in 10 ml of deionized water within constant temperature ovens set at 33 °C and 40 °C, respectively. The temperature was maintained for 10 minutes, after which the solution was analyzed using liquid chromatography-mass spectrometry to quantify the content of amoxicillin penicillin. The same solution samples were also used for antibacterial experiments on solid culture medium inoculated with *Staphylococcus aureus*. Each temperature setting involves three independent replicates. Another group of drug-loaded hydrogel cut into circular disks with a diameter of 2 cm was directly placed on the solid culture medium inoculated with *Staphylococcus aureus* with temperature of 33 °C and 40 °C, respectively, allowing for drug release for the same time. After removing the hydrogel, those samples were put into 37 °C incubator overnight and record the diameter of inhibition zone by ImageJ.

**Text S11. Biocompatibility assessment of the IMT system:** As a demonstration for biocompatibility of the IMT system, histological analysis appears in the *SI Appendix*, Figure S26, with and without application of IMT system, respectively. Tissue slides were obtained from the back skin of rat models after 4-day IMT system attachment. Both results demonstrate normal structure and cellular morphology with no pathological features. The basal cells of the epidermis are neatly arranged and have regular shapes, with no signs of abnormal proliferation or atypical cells. The dermis shows no signs of inflammatory cell infiltration, where collagen fibers are tightly and orderly arranged. Fibroblasts appear in normal numbers with regular morphology, without any observed atypia or proliferation.

**Text S12. Ethics approval:** All human subject studies were approved by the Ethics Committee of Zhongshan Hospital, Fudan University. ID: Y2021073. Informed consent was obtained from all participants involved in this entire study. All animal studies were conducted according to the experimental practices and standards approved by the Animal Welfare and Research Ethics Committee at Fudan University (Approval ID: 202312020S) and Shanghai Yishang Biotechnology Co., Ltd (Approval ID: 2024-Rat-203).

**Text S13. Animal Experiments with the IMT System:** Healthy adult male rats (SD, 6-8 weeks, 180 g - 220 g) were anesthetized with isoflurane and then secured on a surgical table. The hair on their backs was removed using an electric razor and depilatory cream, followed by disinfection with 75% alcohol. A square wound measuring 3 cm x 3 cm was created on the back. After achieving adequate hemostasis, 20 µL of *Staphylococcus aureus* (CMCC26071, Guangdong Microbial Culture Collection Center) solution ( $10^8$  CFU/mL) was selectively injected into the superficial subcutaneous tissue at one corner of the wound using a syringe, while the other part of the wound was left uninfected. The day of modeling was defined as Day 0, with temperature data being tested every other day. During testing, the IMT was applied to the wound and secured with Tegaderm tape (3M) to ensure complete adherence to the wound tissue. After testing, the temperature distribution of the wound was captured using an infrared camera (Seek thermal) for comparison.

Healthy adult male rats (SD, 6-8 weeks, 180-220 g) were acclimated for one week before the experiment. The rats were anesthetized with isoflurane and then secured on a surgical table. The hair on their backs was removed using an electric razor and depilatory cream, followed by disinfection with 75% alcohol. Wounds with a diameter of 8 mm were created on both the left and right sides of the back using a punch. After achieving adequate hemostasis, 20 µL of the *Staphylococcus aureus* (CMCC26071, Guangdong Microbial Culture Collection Center) solution ( $10^8$  CFU/mL) was evenly injected into all wounds. Then, these rats were divided into four groups: (1) the Blank group without IMT system; (2) the Hydrogel group that only involves the drug-loaded



hydrogel patch attached; (3) the IR-LED group that only applies IR-LED illumination on the wound; and (4) the IMT-System group that includes both hydrogel patch and IR-LED on. The wounds in all groups were fixed with Tegaderm film and received various treatment for 1 h. After that, the hydrogel, IR-LED and IMT system were removed and all wounds were covered with Tegaderm film. Optical images of the wounds were taken every day.

On the 4th day, all mice were euthanized, and tissues including the wounds were collected for histological examination. The samples were fixed in 4% paraformaldehyde for over 24 hours, then embedded in paraffin, and sectioned into 4  $\mu\text{m}$  slices. These sections were stained using Hematoxylin and Eosin (H&E), Masson's trichrome, and immunohistochemical staining (CD163, Abcam, #ab182422; CD11b, Abcam, #ab184308; iNOS, Abcam, #ab178945;) to facilitate tissue imaging and analysis. The slides were quickly scanned using a slide scanner (Pannoramic MIDI, 3DHISTECH) to create digital slides covering the entire field of view. The tissue section preparation and staining process were performed with assistance from Shanghai Excellent Doctor Biotechnology Co., LTD. (Shanghai, China). All the statistics were concluded by ImageJ.

#### **Text S14. Remote Wireless Circuit Design and Automated Embedded Program**

**Construction:** The flexible circuit comprised a BLE SoC (nRF 52832, Nordic), a Low-Dropout regulator (TPS7A37, Texas Instruments), four differential amplifiers (INA333, Texas Instruments), four MOSFETs (CSD15571Q2, Texas Instruments), a 2.4 GHz mini antenna (2450AT18A100) and a lithium-ion battery (60 mAh, JieXun). Other components including resistors and capacitors were from Chuangli. The BLE module and instrumentation amplifiers were powered directly by the lithium-ion battery with a Low-Dropout regulator to adjust VCC to 3 V. Each temperature sensor was formed as Wheatstone bridge together with three resistors on the flexible circuit, and the voltage difference was measured using instrumentation amplifiers. The resistance of the bridge arms, the gain of the amplifier, and the reference voltage were all adjustable to ensure the amplifier's output voltage within the measuring range of the ADC. The four MOSFETs were utilized for switching on/off state of IR-LEDs by high/low output of four GPIOs. Each IR-LED was equipped with a resistor connected in series to limit the maximum operating current. The assembled Bluetooth circuit can achieve remote wireless data transmission of more than ten meters. The embedded program was constructed in Keil  $\mu$ Vision IDE and Arduino IDE, which fit to the microcontroller unit with ARM Cortex-M4 processor. To ensure that the processor only makes temperature assessments at the end of the IR-LED pulses, specific adjustments were made in the code, incorporating two timers to choose the right time point.

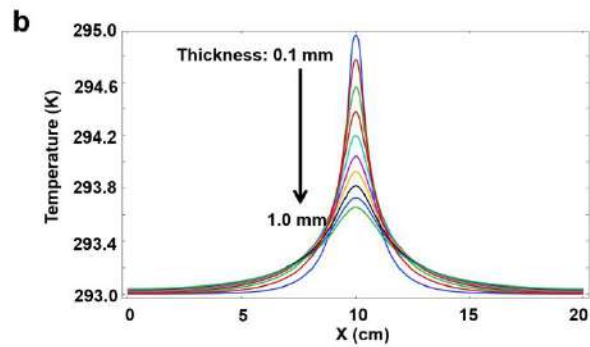
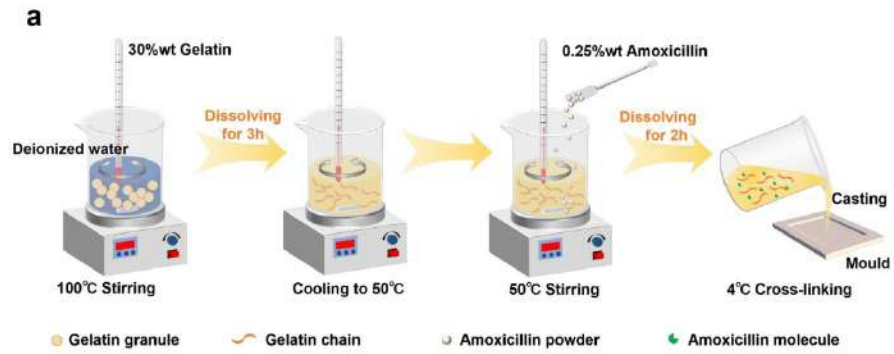


**Fig. S1.** Fabrication of drug-loaded hydrogel. a) The processing schematic of the drug-loaded hydrogel. b) FEA simulation results of thermal isolation effect of the hydrogel with thickness from 0.1 mm to 1 mm.

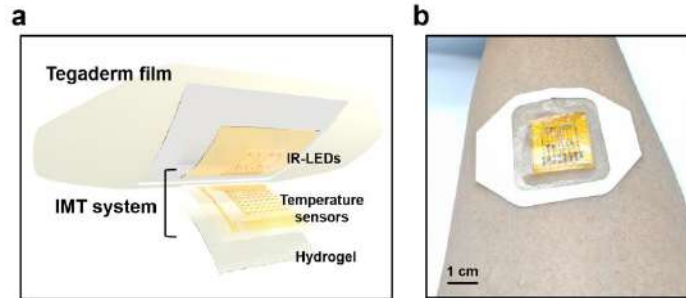


**Fig. S2.** The breathable IMT system with Tegaderm film as encapsulation. (a) Structure illustration of the Tegaderm film served as the encapsulation of the IMT system. (b) Optical image of the IMT system with Tegaderm film as encapsulations.

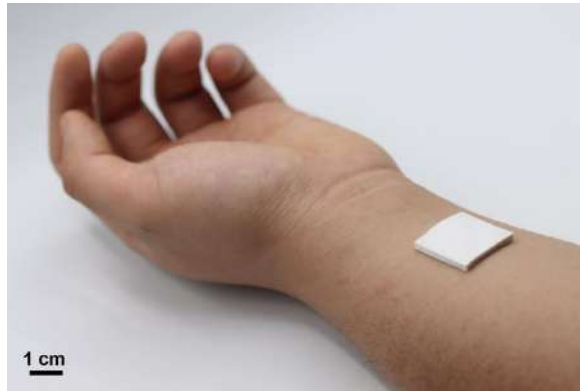


**Fig. S3.** Optical image of the IMT system conformally attached to the forearm of the volunteers.

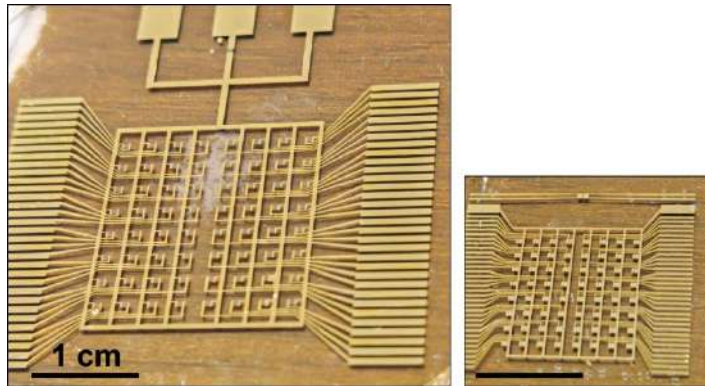


**Fig. S4.** Scalable array design, including sensing area, spatial resolution, channel number, and wire layout.

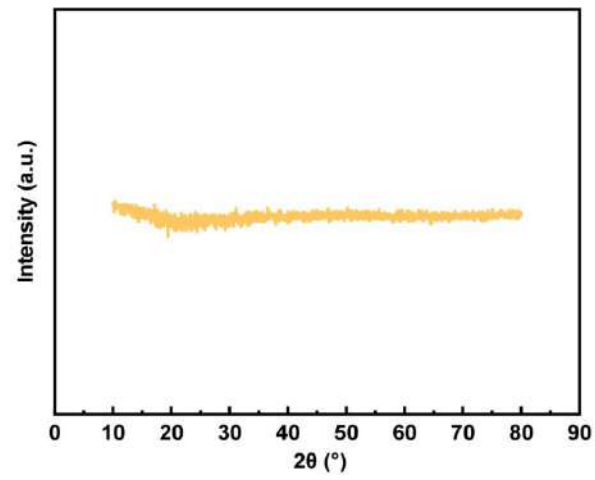


**Fig. S5.** X-ray Diffraction image of amorphous silicon nanomembrane.

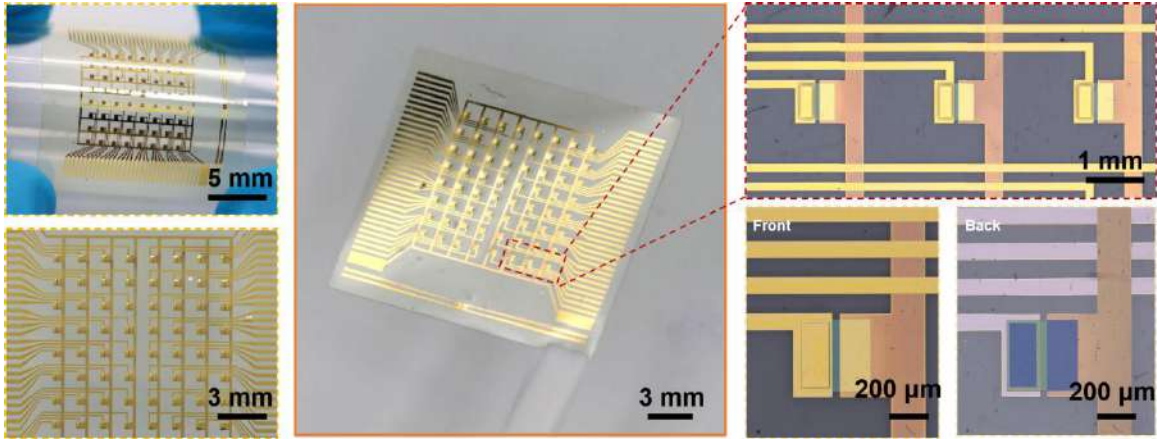
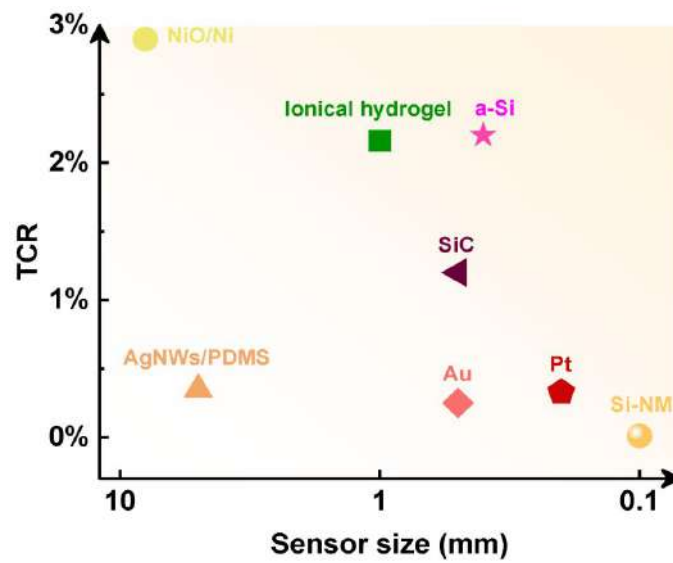
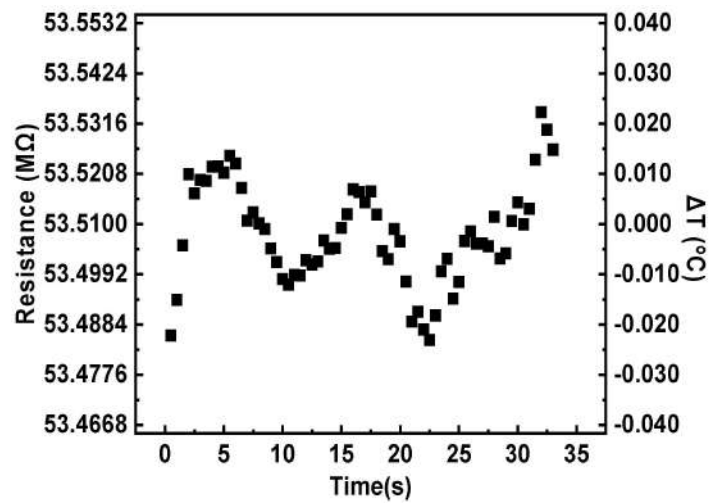


Fig. S6. Optical images of temperature sensor array.



**Fig. S7.** Comparison of the temperature sensor array (a-Si) in this work and the other reported before, demonstrating the superior performance in both sensitivity and spatial resolution. (12, 23-28)





**Fig. S8.** The fluctuation of device resistance (left axis) and converted temperature data (right axis) when the device is placed on a hotplate with constant temperature. The variation of converted temperature data is within 0.1 °C, which is considered as the temperature resolution.

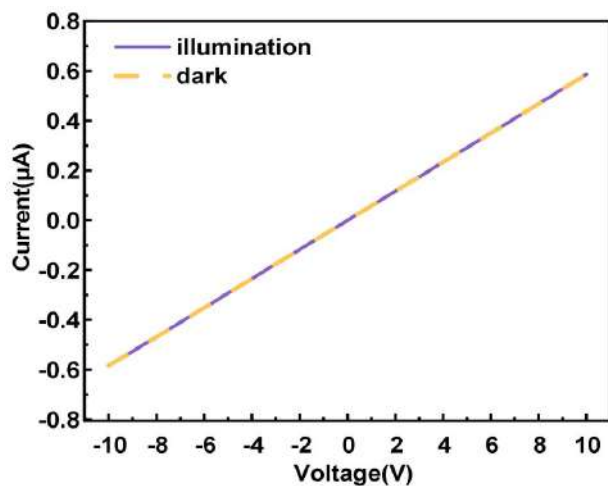


**Fig. S9.** Stable electrical performance of the amorphous-silicon-based temperature sensor under illuminated and dark environment.

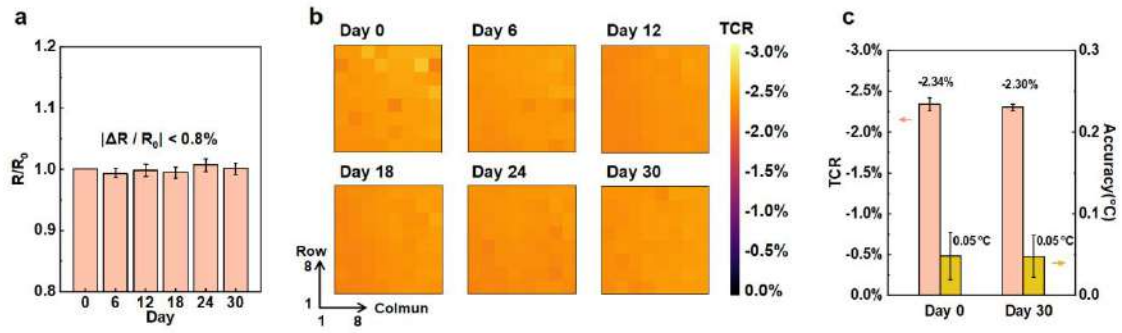


**Fig. S10.** The stable electrical performance of the temperature sensors over extended period. (a) The average resistance of the sensor array maintained over a month.  $R_0$  refers to the resistance of each sensor unit at Day 0. (b) The TCR of the sensor array shows stability over a month. (c) Comparison of TCR and temperature accuracy on Day 0 and Day 30. Error bars represent SD ( $n \geq 3$ ).

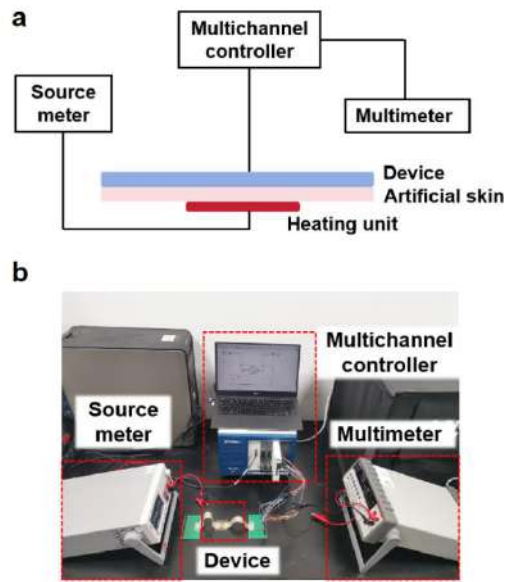


**Fig. S11.** Experimental settings of in vitro validation of temperature sensor array. a) Schematic. b) Settings.

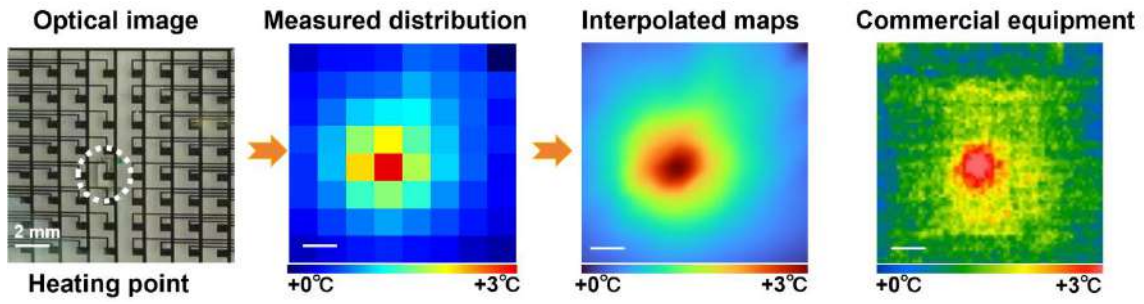


**Fig. S12.** Thermal imaging of the simulating heating spot, with interpolation fitting optimization results consistent with those of a commercial infrared camera.

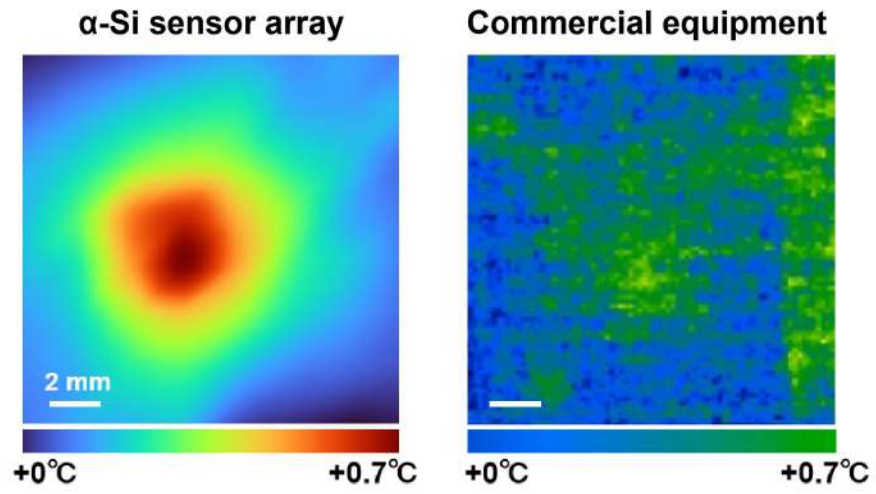


**Fig. S13.** For a temperature difference of 0.7 °C, the α-Si sensor array has better temperature resolution than the commercial infrared camera.

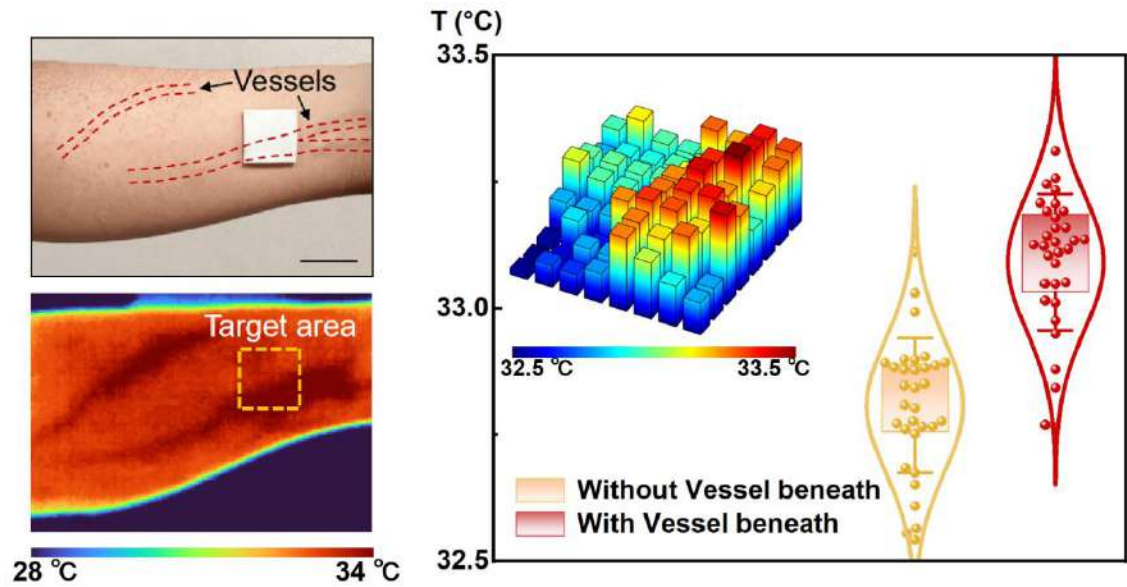


**Fig. S14.** The illustration of the IMT system for localizing the vessel. A) The position of the IMT system and the thermal image showing the vessels site *via* the commercial IR camera. B) Statistics of the temperature data collected by the IMT system. The average temperature readouts of channels near the vessel are apparently higher.

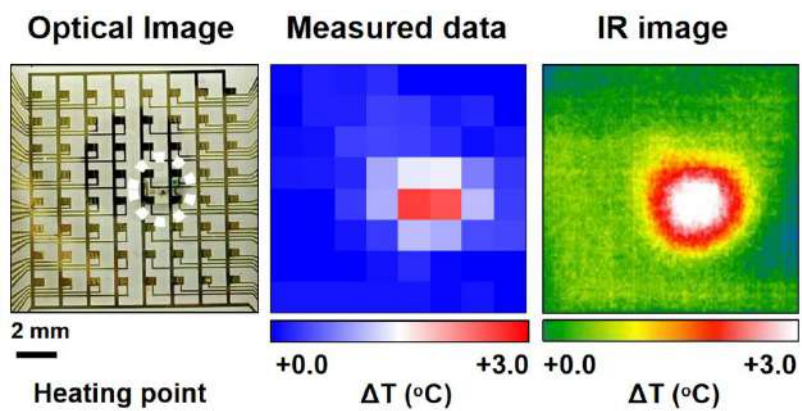


**Fig. S15.** Capability of the sensors to rebuild the temperature profile after 1 month.



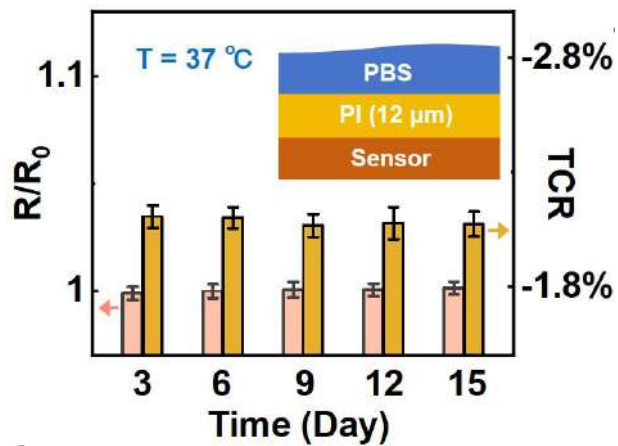


**Fig. S16.** Stable electrical resistance and TCR of temperature sensor array in soaking tests at 37°C.  $R_0$  refers to the resistance of each sensor unit at Day 0.

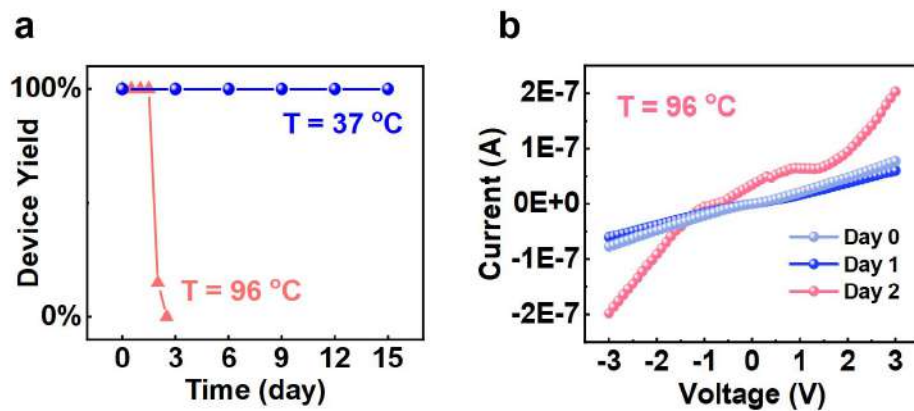


**Fig. S17.** Accelerated soaking test results of the temperature sensors. (a) Device yield of the temperature sensor array in accelerated soaking tests at higher temperatures. (b) I-V curves of a typical temperature sensor at Day 0 to Day 2. The nonlinear I-V curve indicates the device failure caused by vapor permeation.

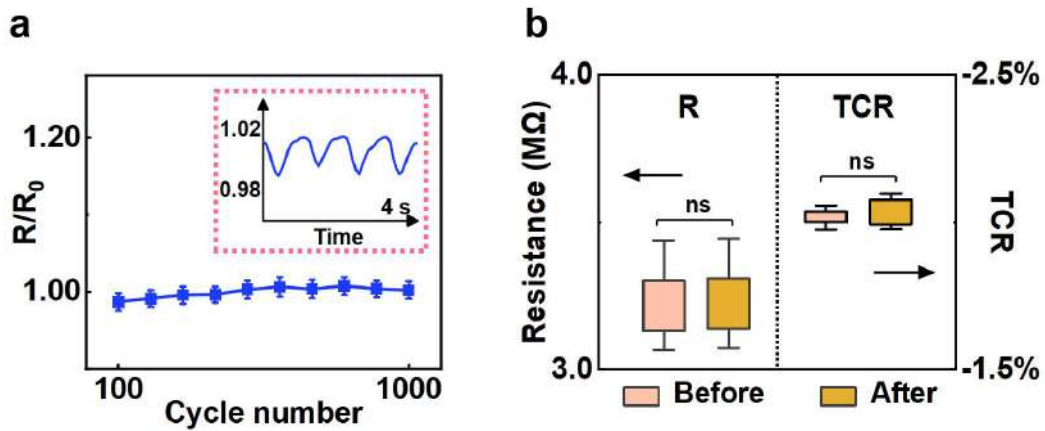


**Fig. S18.** Bending test of the temperature sensor which keeps stable over 1000 cycles. (a) Resistance changes during repeated bending tests.  $R_0$  refers to the average resistance of the sensor. (b) Resistance/TCR change of the 16 sensors before and after 1000-cycle bending.

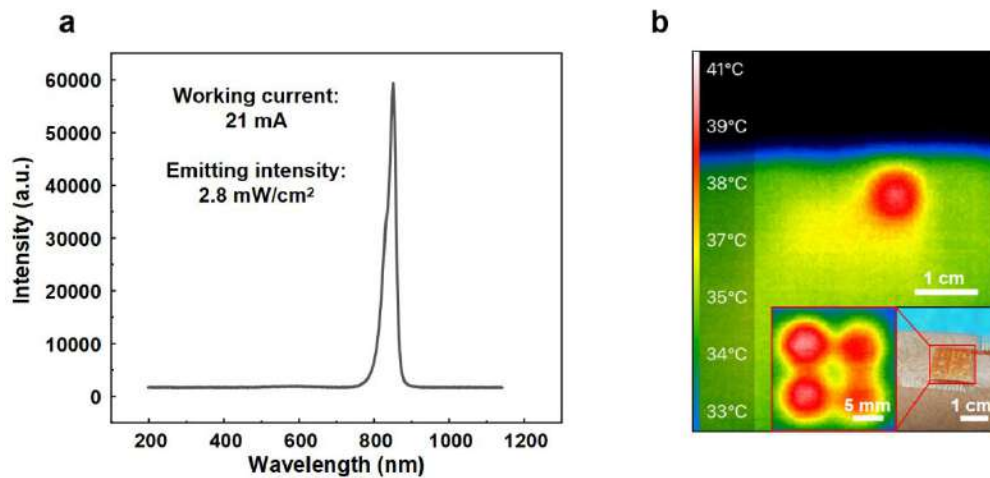


**Fig. S19. Heating IR-LED and its temperature profile.** (a) Spectrum of the IR-LED with an emitting intensity of 2.8 mW/cm<sup>2</sup> at working current of 21 mA. (b) Optical image and IR image of the IR-LED array attached to the human forearm. The inset shows the temperature profile of four IR-LEDs working together.

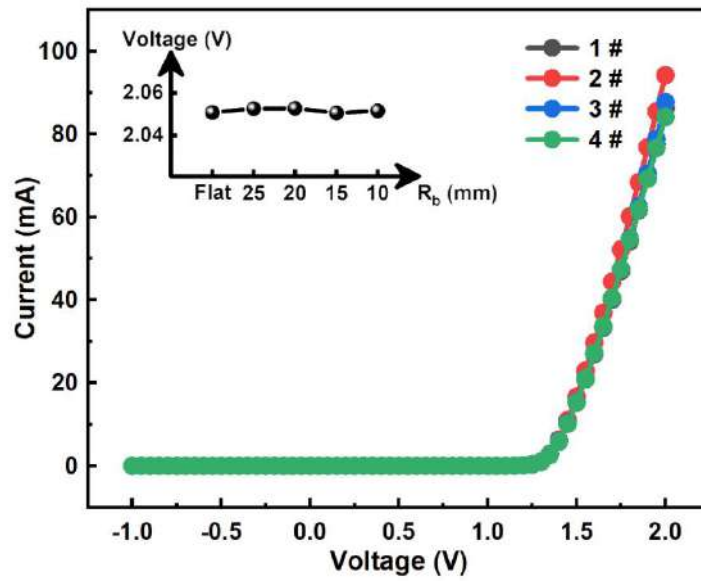


**Fig. S20.** The stable current-voltage curve of four IR-LEDs in a representative array. The inset is the working voltage of the IR-LED operating under constant current mode when bending.

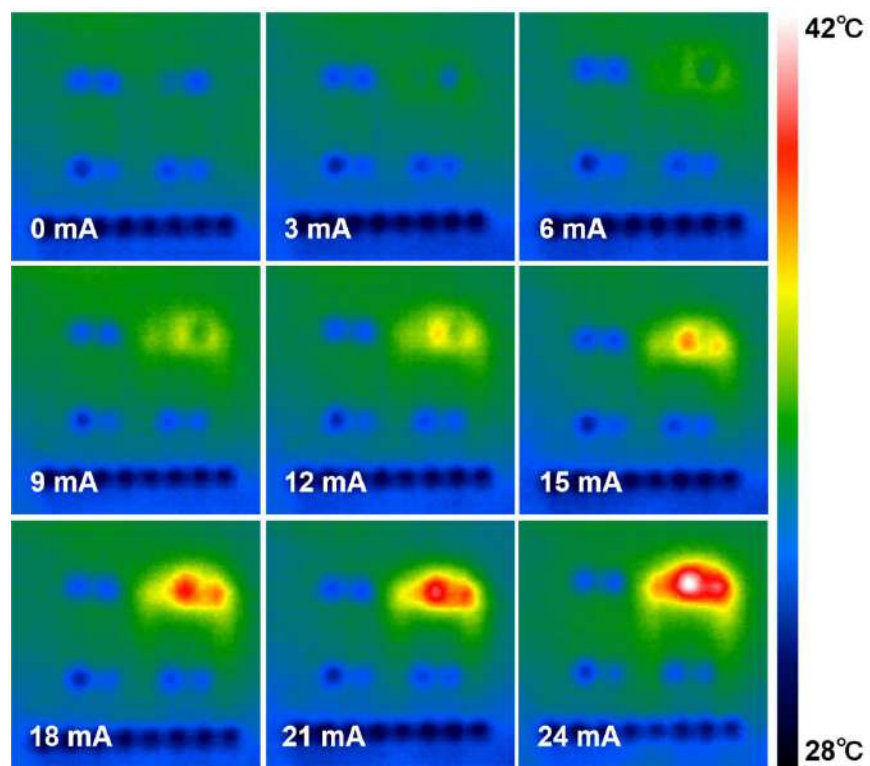


**Fig. S21.** The local temperature increases with the rise in IR-LED operating current.

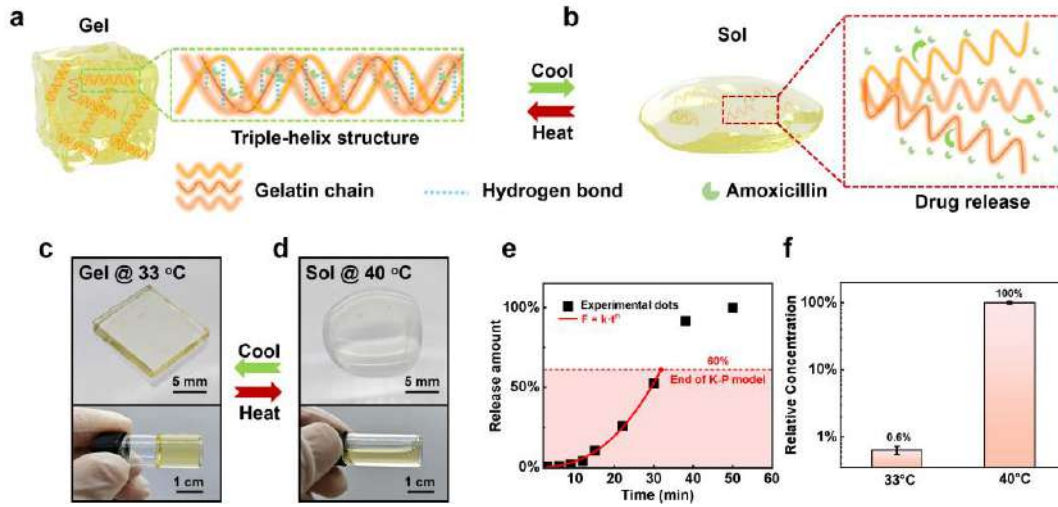


**Fig. S22.** Illustration and analysis of drug release mechanism. (a)(b) Structure of the gelatin hydrogel and heat-triggered drug release at low/high temperatures. (c)(d) Optical images of the hydrogel at 33 °C and 40 °C. (e) The drug release profile of amoxicillin from gelatin hydrogel at 40 °C, which fits the Korsmeyer-Peppas (K-P) model. (f) The comparison of drug release concentration at 33 °C and 40 °C for the same time. Error bars represent SD ( $n \geq 3$ ).

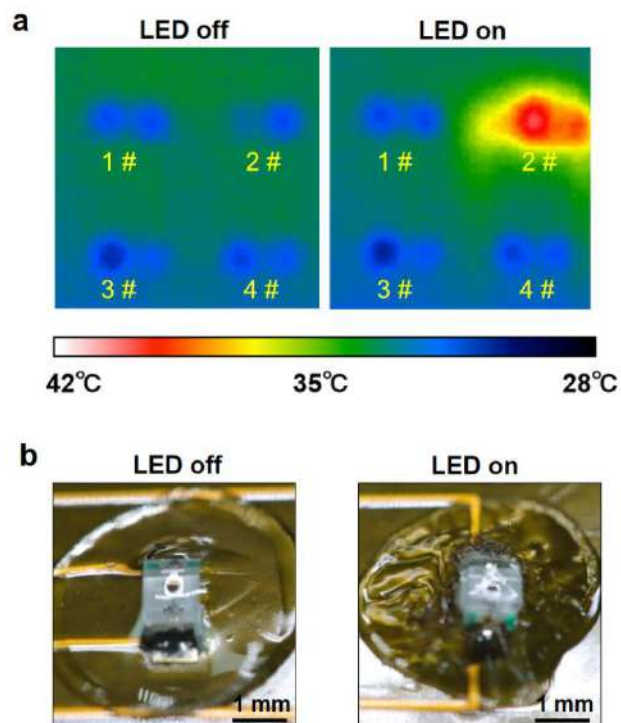


**Fig. S23.** Heat-triggered drug release from hydrogel. a) Thermal image of the IR-LED array. The state of IR-LED 2# is on/off, respectively. b) The hydrogel undergoes sol-gel transition as a result of localized temperature rising.



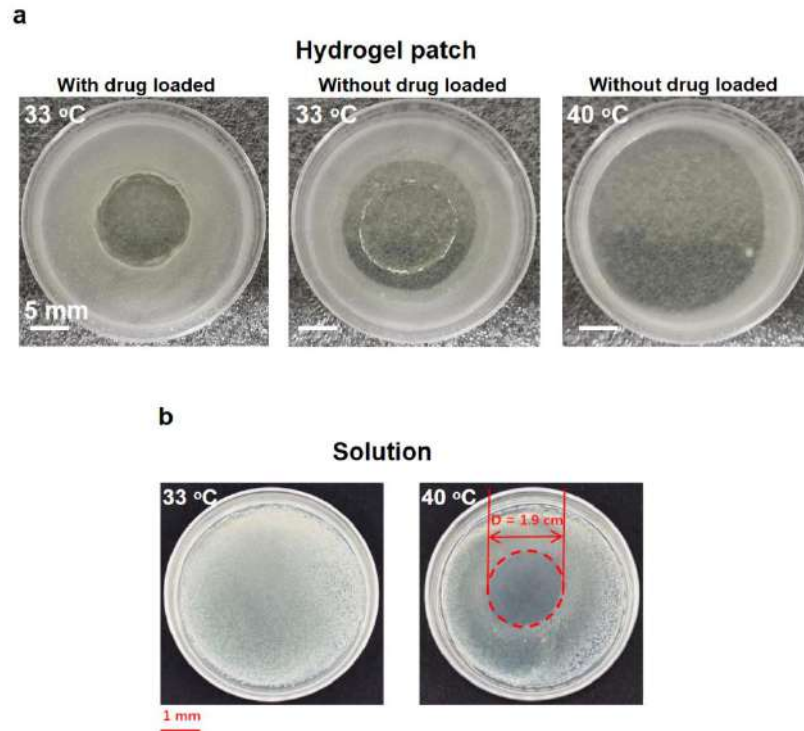


**Fig. S24.** Antibacterial zone results for the effect of drug release of hydrogel in 33 °C and 40 °C respectively. a) Hydrogel patch directly attached to the dish. b) 50  $\mu$ L of solution that containing the released drug is dropped at the center of the dish.

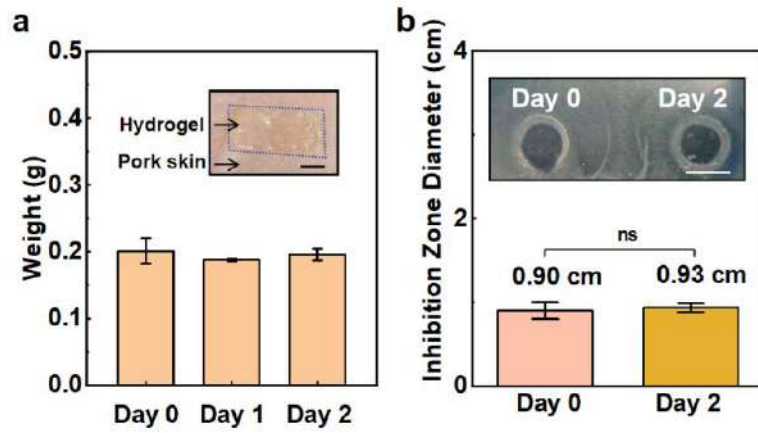


**Fig. S25.** The stability of the hydrogel. (a) The hydrogel weight remains stable on pork skin. Scale bar: 5 mm. (b) The comparable antibacterial ability of the hydrogel patches w/o 3-day attachment on pork skin. The inset shows the inhibition zone photo. Scale bar: 1 cm.

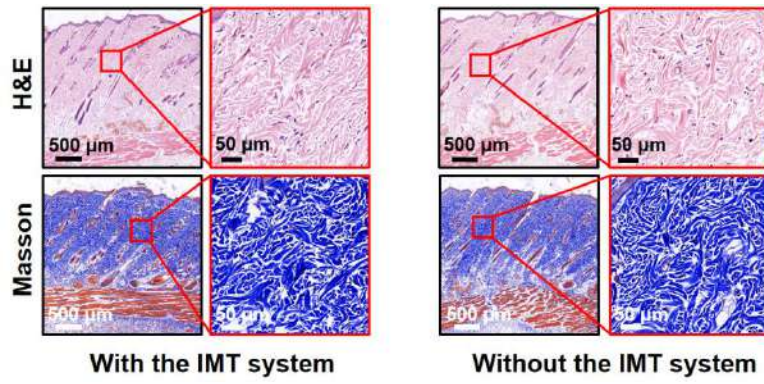


**Fig. S26.** Histological staining results (H&E and Masson) of the bio-tissue with/without the IMT system attached to.

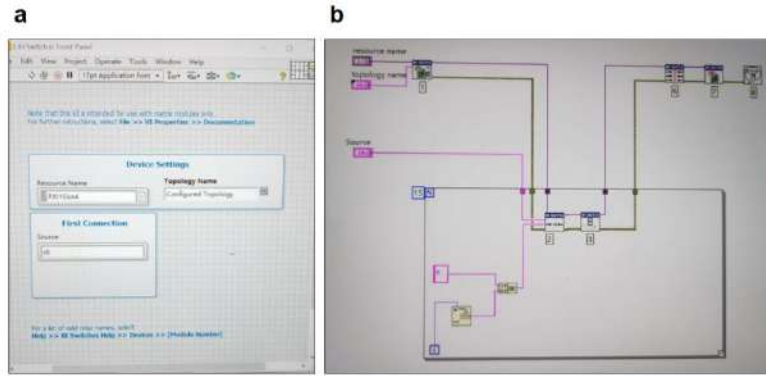


**Fig. S27.** Labview program for the multichannel switcher to address sensor unit by scanning. a) Front panel. b) Program frame.

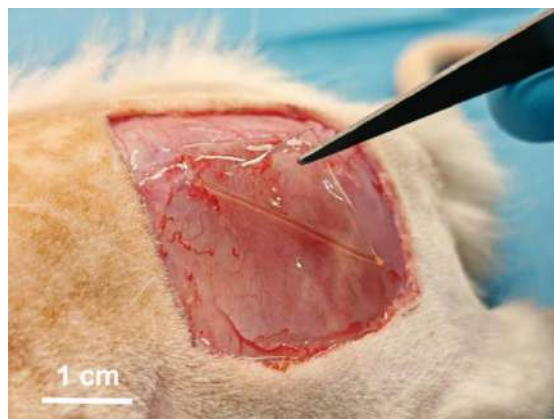


**Fig. S28.** Hydrogel serves as the seamless, robust interface with wound tissues.

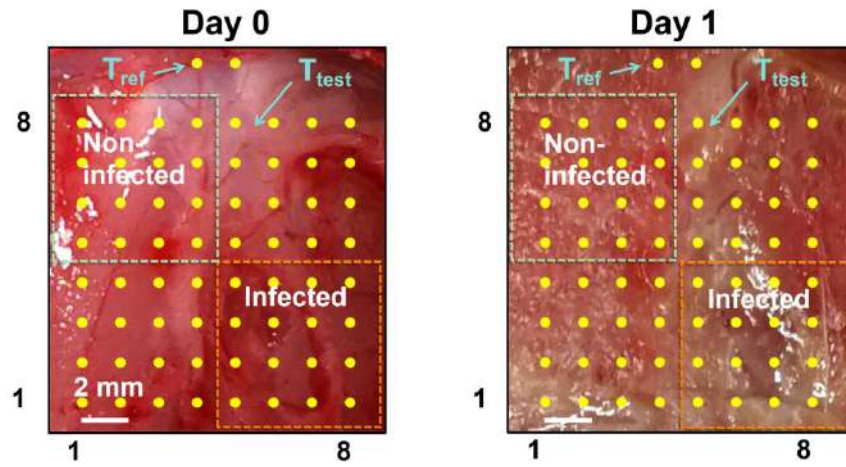


**Fig. S29.** Optical images of large area wound without/with local inflammation on Day 0 and Day 1, respectively.

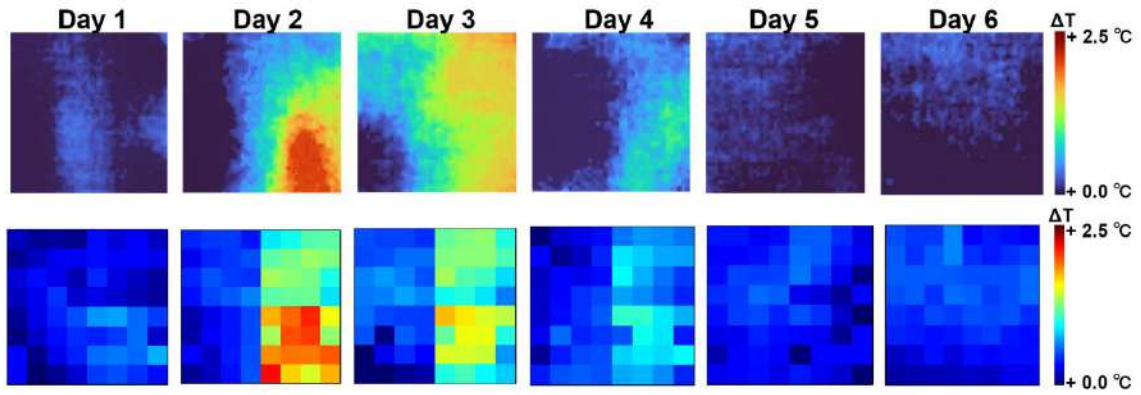


**Fig. S30.** Temperature distribution collected by commercial IR camera (upper) and the IMT system (bottom) cross the wound of the rat over the entire inflammation process.

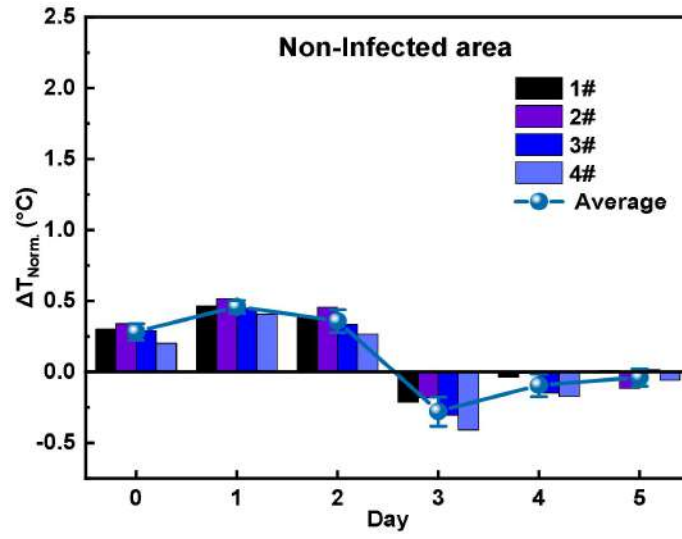


**Fig. S31.** The data of temperature change recorded from four representative channels in the non-infected area.



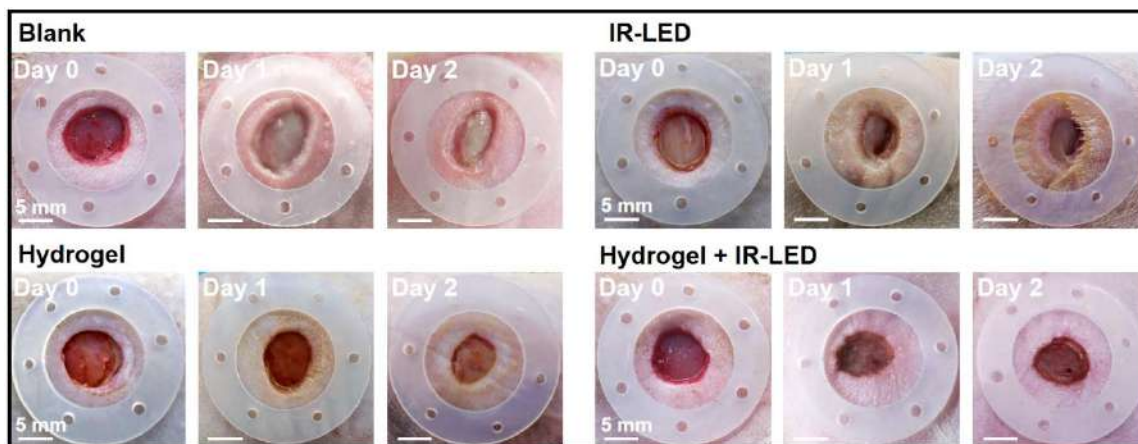


**Fig. S32.** Optical images of the infected wounds. Here, except Group Hydrogel+IR-LED, the others show associated inflammation symptom with signs of moisture and appearance of suppuration.

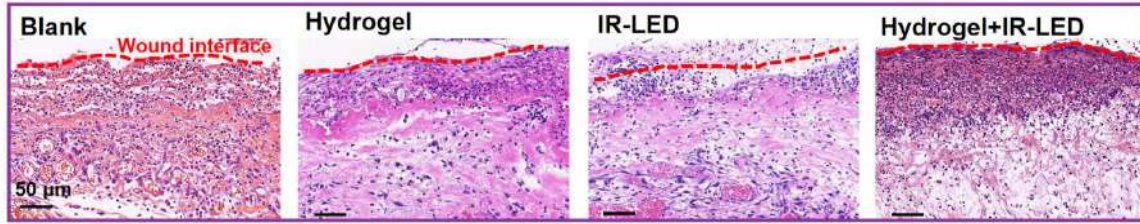


**Fig. S33.** Hematoxylin and eosin (H&E) staining results. There is significantly less eosinophilic granules and more fibroblast migration in Group Hydrogel+IR-LED than those of the other three groups.

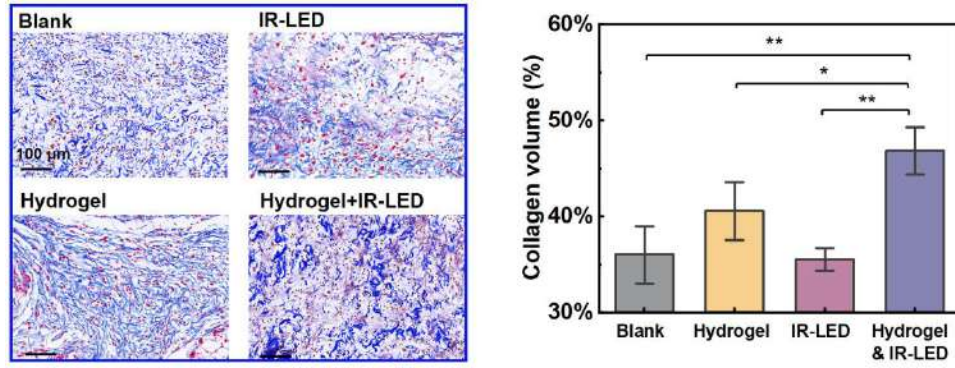


**Fig. S34.** Masson's trichrome staining results and statistics of collagen volume.

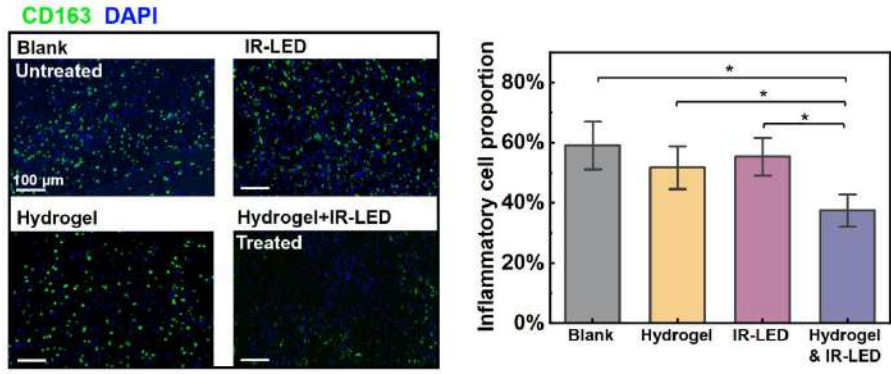


Fig. S35. Immunofluorescence staining results and statistics of inflammatory cell proportion.

**Table. S1.** Recent reports with the localized heating and the comparison of working temperature on biological tissue. NIR: Near Infrared Ray. OLED: Organic Light-Emitting Diode. (29-36)

Reference	Heat source	Wavelength	Temperature	Subject	Function
Miyako et al. <sup>29</sup>	NIR laser	785 nm	42 °C	Nude mouse	Heat shock promoter-mediated gene expression
Zeng et al. <sup>30</sup>	NIR laser	785 nm	45 °C	Female BALB/c mouse	Wound thermal therapy
Chen et al. <sup>31</sup>	NIR laser	808 nm	42 °C	Sprague–Dawley rat	Efficient osteogenesis
Timko et al. <sup>32</sup>	NIR laser	808 nm	42.5 °C	Diabetic rat	Diabetic drug release
Kim et al. <sup>33</sup>	μ-LED	624 nm	36.4-44.1 °C	Tumor xenograft mouse	Photodynamic therapy
Jeon et al. <sup>34</sup>	OLED	600-700 nm	40 °C	Normal human fibroblasts	Photobiomodulation for wound healing
Lee et al. <sup>35</sup>	LED	650 nm	40 °C	Hairless mouse	Trichogenic Photostimulation
Bozkurt et al. <sup>36</sup>	IR-LED	730/805/850 nm	41 °C	Human	Safety assessment of IR-LED
This work	IR-LED	850 nm	40-42 °C	Sprague–Dawley rat	Wound drug release

**Movie S1 (separate file).** Customized Bluetooth app for wireless monitoring.

**Software S1 (separate file).** Code of bicubic interpolation optimization for pixelated temperature mapping data.

## SI References

1. J. Qu et al., Degradable conductive injectable hydrogels as novel antibacterial, antioxidant wound dressings for wound healing. *Chem. Eng. J.* **362**, 548-560 (2019).
2. C. Bisson-Boutelliez, S. Fontanay, C. Finance, F. Kedzierewicz, Preparation and physicochemical characterization of amoxicillin  $\beta$ -cyclodextrin complexes. *AAPS PharmSciTech* **11**, 574-581 (2010).
3. J. R. Grandis et al., Efficacy of topical amoxicillin plus clavulanate/ticarcillin plus clavulanate and clindamycin in contaminated head and neck surgery: Effect of antibiotic spectra and duration of therapy. *J. Infect. Dis.* **170**, 729-732 (1994).
4. J. A. D. Olmo et al., Wound healing and antibacterial chitosan-genipin hydrogels with controlled drug delivery for synergistic anti-inflammatory activity. *Int. J. Biol. Macromol.* **203**, 679-694 (2022).
5. N. M. E. Elsayyad, A. Salama, S. H. Noshi, Concurrent tissue engineering and infection prophylaxis utilising stable dual action amoxicillin loaded scaffolds. *J. Drug. Deliv. Sci. Tec.* **58**, 101788 (2020).
6. S. P. Ndlovu, K. Ngece, S. Alven, B. A. Aderibigbe, Gelatin-based hybrid scaffolds: promising wound dressings. *Polymers* **13**, 2959 (2021).
7. Y. Hong et al., A strongly adhesive hemostatic hydrogel for the repair of arterial and heart bleeds. *Nat. Commun.* **10**, 2060 (2019).
8. A. K. Gaharwar et al., Shear-thinning nanocomposite hydrogels for the treatment of hemorrhage. *ACS Nano* **8**, 9833-9842 (2014).
9. J. Zha, F. Wang, Research progress of high thermal conductivity polyimide dielectric films. *Acta. Phys. Sin.* **71**, 233601 (2022).
10. M. Sang et al., Ultrahigh sensitive Au-doped silicon nanomembrane based wearable sensor arrays for continuous skin temperature monitoring with high precision. *Adv. Mater.* **34**, e2105865 (2022).
11. M. Ahmed et al., Temperature sensor in a flexible substrate. *IEEE Sensors Journal* **12**, 864-869 (2012).
12. R. C. Webb et al., Ultrathin conformal devices for precise and continuous thermal characterization of human skin. *Nat. Mater.* **12**, 938-944 (2013).
13. S. R. Krishnan et al., Epidermal electronics for noninvasive, wireless, quantitative assessment of ventricular shunt function in patients with hydrocephalus. *Sci. Transl. Med.* **10**, eaat8437 (2018).
14. A. Bigi, S. Panzavolta, K. Rubini, Relationship between triple-helix content and mechanical properties of gelatin films. *Biomaterials* **25**, 5675-5680 (2004).
15. L. Guo, R. H. Colby, C. P. Lusignan, T.H. Whitesides, Kinetics of triple helix formation in semidilute gelatin solutions. *Macromolecules* **36**, 9999-10008 (2003).
16. D. Hellio, M. Djabourov, Physically and chemically crosslinked gelatin gels. *Macromol. Symp.* **241**, 23-27 (2006).
17. R. W. Kormeyer et al., Mechanisms of solute release from porous hydrophilic polymers. *Int. J. Pharm.* **15**, 25-35 (1983).
18. P. L. Ritger, N. A. Peppas, A simple equation for description of solute release II. Fickian and anomalous release from swellable devices. *J. Control. Rel.* **5**, 37-42 (1987).
19. N. A. Peppas, J. J. Sahlin, A simple equation for the description of solute release. III. Coupling of diffusion and relaxation. *Int. J. Pharm.* **57**, 169-172 (1989).
20. J. M. Llabot, R. H. Manzo, D. A. Allemandi, Drug release from carbomer:carbomer sodium salt matrices with potential use as mucoadhesive drug delivery system. *Int. J. Pharm.* **276**, 59-66 (2004).

21. K. V. Ranga Rao, K. P. Devi, Swelling controlled-release systems: recent developments and applications. *Drug. Dev. Ind. Pharm.* **14**, 2299-2320 (1988).
22. C. Ferrero, A. Muñoz-Ruiz, M. R. Jiménez-Castellanos, Fronts movement as a useful tool for hydrophilic matrix release mechanism elucidation. *Int. J. Pharm.* **202**, 21-28 (2000).
23. J. Shin *et al.*, Sensitive wearable temperature sensor with seamless monolithic integration. *Adv. Mater.* **32**, 1905527 (2020).
24. K. Sim *et al.*, An epicardial bioelectronic patch made from soft rubbery materials and capable of spatiotemporal mapping of electrophysiological activity. *Nat. Electron.* **3**, 775-784 (2020).
25. J. Zhang *et al.*, Mechanically robust, flexible, fast responding temperature sensor and high-resolution array with ionically conductive double cross-linked hydrogel. *Adv. Funct. Mater.* **34**, 2314433 (2024).
26. H.-P. Phan *et al.*, Long-lived, transferred crystalline silicon carbide nanomembranes for implantable flexible electronics. *ACS Nano* **13**, 11572-11581 (2019).
27. J. J. Kim, G. R. Stafford, C. Beauchamp and S. A. Kim, Development of a dental implantable temperature sensor for real-time diagnosis of infectious disease. *Sensors* **20**, 3953 (2020).
28. S. K. Kang *et al.*, Bioresorbable silicon electronic sensors for the brain. *Nature* **530**, 71-76 (2016).
29. E. Miyako, T. Deguchi *et al.*, Photothermic regulation of gene expression triggered by laser-induced carbon nanohorns. *Proc. Natl. Acad. Sci. U.S.A.* **109**, 7523-7528 (2012).
30. Z. Zeng *et al.*, Thermal-cascade multifunctional therapeutic systems for remotely controlled synergistic treatment of drug-resistant bacterial infections. *Adv. Funct. Mater.* **34**, 2311315 (2024).
31. Y. Chen *et al.*, Superior synergistic osteogenesis of Mxene-based hydrogel through supersensitive drug release at mild heat. *Adv. Funct. Mater.* **34**, 2309191 (2024).
32. B. P. Timko *et al.*, Near-infrared-actuated devices for remotely controlled drug delivery. *Proc. Natl. Acad. Sci. U.S.A.* **111**, 1349-1354 (2013).
33. K. Kim *et al.*, Fully implantable and battery-free wireless optoelectronic system for modifiable cancer therapy and real-time monitoring. *npj Flex. Electron.* **7**, 41 (2023).
34. Y. Jeon *et al.*, A wearable photobiomodulation patch using a flexible red-wavelength OLED and its in vitro differential cell proliferation effects. *Adv. Mater. Technol.* **3**, 1700391 (2018).
35. H. E. Lee *et al.*, Trichogenic photostimulation using monolithic flexible vertical AlGaInP light-emitting diodes. *ACS Nano* **12**, 9587-9595 (2018).
36. A. Bozkurt, B. Onaral, Safety assessment of near infrared light emitting diodes for diffuse optical measurements. *Biomed. Eng. Online* **3**, 9 (2004).